Journal of the Meteorological Society of Japan

EARLY ONLINE RELEASE

The DOI for this manuscript is
DOI:10.2151/jmsj.2025-020
J-STAGE Advance published date: February 28, 2025
The final manuscript after publication will replace the preliminary version at the above DOI once it is available.

The Climatological Features of Atmospheric Rivers and their Role in Water Vapor Transport in the South Polar Region

Kazu TAKAHASHI[1]

The Graduate University for Advanced Studies, Tokyo, Japan

and

Takatoshi SAKAZAKI

Graduate School of Science, Kyoto University, Kyoto, Japan

Jun *, 2024

----

1) Corresponding author: Kazu Takahashi, Department of Polar Science, School of Multidisciplinary Sciences, The Graduate University for Advanced Studies, 10-3, Midori-cho, Tachikawa-shi, Tokyo 190-0031 JAPAN
Email: takahashi.kazu@nipr.ac.jp

Tel: +81-42-512-0759

Abstract

In recent years, Atmospheric Rivers (ARs) have been recognized to influence the Antarctic ice sheet via extreme snowfall, latent and sensible heat transports, and anomalous changes in radiation balance. ARs are defined as extreme moisture transport events and are thought to account for a significant fraction of total moisture transport from mid to high-latitude regions, such as Antarctica. While previous studies have investigated ARs associated with extreme events over Antarctica and the Southern Ocean, their climatological features remain poorly understood. We investigate the climatology of ARs in the south polar region such as their geographical distribution and their role in moisture transport, by using an AR detection method that extracts the area with a localized moisture transport at 6-hourly intervals for JRA55. Notably, our method effectively describes the geographical distribution of ARs, contrasting with conventional methods that use temporal fixed criteria. We find that the contours of climatological AR frequency display a zonally asymmetric, spiral-like structure extending from mid-latitudes in the Atlantic to high-latitudes in the Pacific Ocean. This distribution produces a zonal asymmetry in meridional moisture transport, which may contribute to the observed zonally asymmetric distribution of Antarctic precipitation. We also suggest that the dominant meteorological systems associated with the ARs differ geographically: extra-tropical cyclones in the Atlantic and blocking events in the Pacific Oceans. At 60°S, we find that the AR detection number has not had a significant trend over recent decades, but the typical intensity of individual ARs in austral summer has increased over the last 41 years.

Keywords Atmospheric river; Antarctica; Southern Hemisphere; Moisture transport

1. Introduction

The American Meteorological Society Glossary defines an atmospheric river (AR) as "a long, narrow and transient corridor of strong horizontal water vapor transport". A typical AR is developed along a low-level jet stream ahead of the cold front of an extra tropical cyclone (Ralph et al., 2004, 2017a, 2017b) and sometimes causes extreme precipitation events in midlatitudes (Newell et al., 1992; Zhu and Newell, 1994, 1998; Neiman et al., 2007; Ralph et al., 2004, 2013, 2017a; Ralph and Dettinger, 2011; Mundhenk et al., 2016). The AR also plays a significant role in poleward moisture transport: it was reported that ARs accounted for a significant fraction (more than 90%) of poleward atmospheric water vapor flux in the midlatitudes (e.g., Zhu and Newell, 1998; Nash et al., 2018).

Most previous studies of AR have considered extratropical regions, such as the west coast of North America and the northwest Pacific, where extratropical cyclones are most active (e.g. Ralph et al., 2004, 2017b; Mundhenk et al., 2016, Kamae et al., 2017). By contrast, the polar region (esp. Antarctica), which is the focus of this study, has received much less attention until 2010s. However, many recent studies have highlighted the importance of AR for the variability of ice sheet mass on and sea ice growth around Antarctica with case studies (e.g. Gorodetskaya et al., 2014; Wille et al., 2019, 2022, 2024a, 2024b; Francis et al., 2020; Terpstra et al., 2021; Gerhring et al., 2022) and with statistical approaches (e.g. Wille et al., 2021; Maclennan et al., 2022; Baiman et al., 2024). The Antarctic surface ice mass accounts for more than 90% of total fresh water on this planet so that its variability has a crucial role in climate change including global sea level trends (Church and Gregory, 2001; Shepherd and Wingham, 2007; Wingham et al., 2006).

The annual precipitation in Antarctica, which contributes to the Antarctic surface ice mass balance, is largely accounted for by intensive precipitation events occurring only a few times per year (Fujita and Abe, 2006; Turner et al., 2019). It has been pointed out that such intensive snowfall is typically accompanied by large water vapor flux associated with extratropical cyclones and/or blocking events (Hirasawa et al., 2000; Sinclair and Dacre, 2019). Wille et al. (2021) suggested that such events were caused by ARs associated with blocking episodes. Gorodetskaya et al. (2014) also demonstrated that the snow accumulation events related to ARs account for about 70% of annual precipitation at locations in East Antarctica. Note that an AR sometimes can act to decrease (melt) the surface ice due to its Foehn effects and/or the enhanced downward longwave radiation from the associated clouds (Bozkurt et al., 2019; Wille et al., 2019, 2022).

It has been reported that there is a large geographical dependence (zonal asymmetry) in annual precipitation over Antarctica (Vaughan et al., 1999; Bromwich et al., 2004). Notably, Bromwich et al. (2004) showed that the western part of Antarctica had more precipitation than the eastern part. The AR activity and the associated moisture transport were, by contrast, reported to be zonally symmetric in the south-polar region (Nash et al., 2018; Wille et al., 2021). Wille et al. (2021) showed that the AR detection frequency was a few days per year at every longitude over the Southern Ocean (see their Fig. 1). Nash et al.

(2018) reported that the moisture transport component due to ARs showed less longitudinal variation than the total transport.

Given the large contribution of ARs to the annual precipitation over the south polar region, how can we reconcile this apparent contradiction in the zonal symmetry of the distribution between surface precipitation and AR detection frequency? Here, it should be noted that Nash et al. (2018) and Wille et al. (2019, 2021, 2022) defined an AR as an area where the integrated water vapor transport (IVT) is larger than some temporally fixed climatological threshold defined at "each grid point" (e.g. 98th percentile). Indeed, among various algorithms proposed for the AR detection (see Shields et al., 2018 and Rutz et al., 2019, for summary) the methods utilizing spatially dependent criteria, as adopted by Nash et al. (2015) and Wille et al. (2021), have been commonly used for recent studies. These algorithms aim at detecting the area where the IVT is high compared to its local climatology (Guan and Waliser, 2015; Wille et al., 2019), Unfortunately, these may not be suitable for examining the geographical distribution of AR frequency, since the number detected has an upper limit by definition (e.g., when the 98th percentile value in IVT at each grid point is used for detection, the frequency should be the same (i.e., 2%) for all grid points when long data sets are analyzed) (see Appendix A for details including Fig. A1). This limitation of these methods has been pointed out by Maclennan et al. (2022).

The detection method employed may also affect the results for long-term trends in AR frequency. For example, Wille et al. (2019), found that the number of ARs detected showed a positive trend over several decades. However, such trend may just reflect an observed positive trend in zonal-mean, background IVT (Fig. 1b); that is, because they used the temporally fixed threshold for AR detection, more ARs would tend to be detected in recent years by this method.

We also note that the number of AR “detections” may not simply indicate the actual number of AR “occurrences”. If an AR stays at the same location (grid) over several time steps, it may be counted multiple times in a conventional detection algorithm. Thus, it should be worthwhile to apply a tracking for AR objects and count the actual number of AR occurrences (e.g., Payne and Magnusdottir, 2014; Zhou et al., 2018; Gonzales et al., 2019; Guan and Waliser, 2019). Note that, as far as we know, there are few studies that performed such AR tracking for southern polar region.

The original notion of an AR is a literally river-like, spatially localized structure of IVT. The purpose of this study is to elucidate the climatological features of ARs over the south-polar region, using an AR detection algorithm that uses a temporally variable threshold and, thus, is appropriate for extracting such spatially extreme objects at each time step. We will apply this method to revisit the geographical distribution and long-term trends for AR activity and to determine how the results differ from previous studies that used temporally fixed, spatially dependent threshold for AR detection. Here, we adopt a rather simple method proposed by Zhu and Newell (1998), in which an AR is defined at an individual time step as an area that has anomalous IVT on each latitude belt (see Sec. 2 for details). It will be demonstrated that the AR frequency shows a rather zonally asymmetric distribution. Furthermore, AR tracking is performed to determine how much the number of detections reflects the actual number of AR occurrences and the persistence (i.e., the tendency to stay at the position) for occurrences.

The seasonality,the long-term trend, and the interannual variability of AR frequency will also be discussed. AR activity is associated with the Southern Annual Mode (SAM) and Pacific South American mode 2 (PSA2), which are modes of interannual variability (Wille et al., 2021; Shields et al., 2022), and the correlation depends on the location (Wille et al., 2021). It has been reported that SAM has a positive long-term trend, especially in austral summer (Thompson and Solomon, 2002; Marshall, 2003), corresponding to the poleward shift of extratropical westerlies (Chen and Held, 2007) and that this leads to the poleward shifts of storm trucks and ARs (Chemke, 2022; Li and Ding, 2024).

This paper is organized as follows. In section 2, we describe the dataset and methodology used to detect and track ARs. Section 3 shows the geographical distribution of AR and its contribution to the zonal asymmetry in meridional moisture transport. In Section 4, the synoptic meteorological factors contributing to the AR detection/occurrence distribution, notably the storm track and atmospheric blocking, are discussed. The interannual variability of AR frequency is also examined in terms of its relationship with the predominant atmospheric internal variability modes such as SAM and PSA. Section 5 summarizes the main findings.

2. Data and Method

2.1 Reanalysis data

We use the Japanese 55-year Reanalysis (JRA-55) data (Kobayashi et al., 2015), which provides global, 6-hourly atmospheric fields with a longitude-latitude resolution of 1.25 °-1.25° and on 41 vertical levels (20 levels below 300 hPa). Data over 41 years between 1980 and 2020 are analyzed. Wille et al. (2019, 2021) demonstrated that similar results of AR detection were obtained when their algorithm was applied to different reanalysis: JRA-55, ERA5 (European Centre for Medium-Range Weather Forecasts v5 reanalysis) (Herbach et al., 2020), MERRA-2 (The Modern-Era Retrospective analysis for Research and Applications, version 2), and CFSR (Climate Forecast System Reanalysis). As part of our study, we confirmed that the horizontal distribution of AR detection using our algorithm (c.f., Fig. 3) was similar between JRA-55 and ERA5 (Fig. S1).

2.2 AR detection algorithm

There are many types of AR detection algorithms proposed in previous studies (Shields et al., 2018; Rutz et al., 2019), though it is common to regard a large, narrow IVT area as an AR. As noted in the Introduction, most recent studies used a method that set different IVT thresholds for individual horizontal grid points. Here, we instead adopt a rather simple method originally proposed by Zhu and Newell (1998) with a slight modification for the present purpose. Notably, their method aimed to find any narrow, large IVT areas at each time step. They showed that the areas identified by their algorithm basically agreed with those determined by a visual (subjective) search for such localized, anomalous areas. Detailed procedures in the algorithm as we applied it are now described below. First, the IVT is defined and calculated as the magnitude of the vertically integrated water vapor flux from the surface to 300hPa:

$$\boldsymbol{IVT} = \sqrt{\left(\boldsymbol{g^{-1}} \int_{\boldsymbol{sfp}}^{\boldsymbol{300hPa}} \boldsymbol{uq\,dp}\right)^{\boldsymbol{2}} + \left(\boldsymbol{g^{-1}} \int_{\boldsymbol{sfp}}^{\boldsymbol{300hPa}} \boldsymbol{vq\,dp}\right)^{\boldsymbol{2}}} \quad (2.2.1)$$

Here, *q* is specific humidity ($\mathrm{kg\,kg^{-1}}$), *u* and *v* are zonal and meridional wind velocity ($\mathrm{m\,s^{-1}}$), respectively, *sfp* is the surface pressure, and *g* (=9.80665 $\mathrm{m\,s^{-2}}$) is the gravitational acceleration.

Second, we detect areas where the IVT exceeds 30% of the maximum zonal anomaly of IVT at each latitude (Zhu and Newell, 1998). Of these objects, we then select ones which meet two geometric criteria: 1) length >2000 km, and 2) ratio of length to width >2 (Guan and Waliser, 2015). Here we define the length as the distance between the two most distant grid cells included in the object. The width is calculated as the area divided by its length. Note that the two geometric criteria implicitly require that the width be larger than 1000 km. Finally, if the IVT averaged over the object exceeds 100 $\mathrm{kg\,m^{-1}s^{-1}}$, we regard the object as an AR (c.f. Guan and Waliser, 2015). We chose this rather low threshold of IVT because of the typically low moisture content in the polar regions. Figure 1a shows the latitudinal distribution of zonal mean IVT for the recent four decades. We indeed see that IVT is usually very small, being less than 50 $\mathrm{kg\,m^{-1}s^{-1}}$, poleward of 65°S.

Fig. 1

To study the sensitivity to the parameters used for detection, we compared AR detection frequency to that based on the difference percentage of the threshold and geometric requirements. While the different percentages of the threshold do not affect the result of AR detection quantitatively, the geometric requirements are necessary for detecting meridionally elongated objects (i,e, a river-like structure) (see Appendix B for details) (Fig. 3, B1, and B2).

A strong point of the present method is that the detected objects basically have characteristics of the original notion of AR (i.e., a river-like structure) (Zhu and Newell, 1998). Note that the results with the present method are insensitive to the climatological trend of background moisture transport. Figure 1b shows the time evolution of the annual, zonal mean IVT at each latitude, while Figure 1c shows their linear trends. Between 40°S and 65 °S, where the zonal mean IVT is large, the mean IVT does not change much over the 1980s and 1990s, while it slightly increased after that, particularly for the most recent decade (Fig. 1b). As a result, the zonal mean IVT shows a significant, increasing trend between 40°S and 65°S (Fig. 1c). For this situation, as noted in Introduction, the AR algorithms that use a temporally fixed threshold would tend to detect more ARs in recent years. By contrast, the present algorithm extracts a localized IVT area at each time step, and thus the trend in AR detection "frequency", if any, should be little affected by this factor, though the individual AR "intensity" (the magnitude of IVT in each AR) could change. Fig. 2

Figure 2 shows examples of ARs detected on May 6th-8th, 2019 (a-c) and January

17th-19th,1980 (d-f) as detected by the present algorithm. We see that these ARs have long narrow structures, with humid air intruding from low to high latitudes. The ARs for the first case (Figs. 2a-c) move eastward, with their water vapor flux being eastward or southeastward. On the other hand, the ARs for the second case (Figs. 2d-f) persist at almost same position and transport water vapor poleward (Figs. 2d-f). Such a difference will be discussed later in Secs. 3 and 4.

2.3 AR tracking

To count the actual number of AR occurrences, an AR-tracking analysis is performed. If an AR at one time step overlaps the AR at the next time step by more than 10%, the two objects are regarded as the same one. Considering that a typical AR moves ~100 km over 6 hours (one time step of the dataset) (a typical speed is 6 $\mathrm{m\,s^{-1}}$; Newell et al., 1992) and the width of detected AR is always >1000 km by the geometric criteria for detection (Sec. 2.2), the overlapping ratio of the two objects at adjacent time steps should be >10%. Repeating this operation, we can track an AR from its origin to termination. The number of tracks is thus the number of AR "occurrences". We also calculate the persistence of an AR at each grid point as the number of AR detections divided by that of AR occurrence.

An AR sometimes separates into several ARs and sometimes merges with other ARs. For separation, all "child" ARs are regarded as the same one as the "mother" AR (the AR occurrence remains one after the separation). For the merger, the one whose "age" (the period from the generation to the merger) is the oldest is identified as the one that continues after the merger. On the other hand, the other younger ARs merged into the AR are regarded as terminated one-time step before the AR merger. The treatment of merger and separation is different from that of previous studies.

One example of AR tracking is shown in Figs. 2a-c. We find that a relatively small AR located at about 30°E between 20°S and 30°S at 06 UTC on May 6th, moves eastward with time while developing (denoted by a green arrow). These ARs are indeed regarded as the same one by our tracking method, as seen by gray contours which show the outline of the footprint of this AR over 78 hours of the tracking period. This outline indicates that the AR occurred at the south of African continent, moved southeastward and then terminated in the south of Australia.

2.4 Storm track identification

The storm track is the region where the synoptic-scale Eddy Kinetic Energy (EKE) reaches its maximum (Inatsu and Hoskins, 2004). In this study, EKE is calculated as

$$EKE = \frac{1}{2}\left(\overline{u}^{*2} + \overline{v}^{*2}\right), (2.4.1)$$

where u and v are the zonal and meridional winds, respectively, the asterisk denotes the zonal anomaly and $\overline{F_{(t)}}$ is the synoptic-scale component of F (u or v) at time *t* (Inatsu and Hoskins, 2004), which is obtained as;

$$\overline{F_{(t)}} = \sum_{k=-5}^{5} a_{|k|} F_{(t+k\ \mathrm{day})}\,.$$

Here, $F_{(t+k\ day)}$ is the daily mean quantity, while $(a_1, a_2, a_3, a_4, a_5) = (0.7, -0.25, -0.15, 0.042, 0.041, 0.057)$.

2.5 Blocking high detection

Blocking highs are detected in the region between 45°S and 70°S, basically following the methods applied for the blocking high in the Northern Hemisphere, which were proposed by Barriopedro et al. (2006) and Kazamoto (2008). At each grid point with its longitude and latitude being λ and φ, respectively, the meridional geopotential height gradients on the north side (GHGN) and the south side (GHGS) are calculated as;

$$GHGN = \frac{Z_{(\varphi_0,\lambda)} - Z_{(\varphi_n,\lambda)}}{\varphi_n - \varphi_0},$$

$$GHGS = \frac{Z_{(\varphi_s,\lambda)} - Z_{(\varphi_0,\lambda)}}{\varphi_0 - \varphi_s},$$

where $Z_{(\varphi,\lambda)}$ denotes the daily mean geopotential height and,

$$\varphi_n = \varphi_0 + 20°,$$

$$\varphi_s = \varphi_0 - 17.5°. \ (2.5.2)$$

If the following requirements are met over some days (*n* days), it is determined that a blocking high is occurring on the grid point;

$$GHGN > 0,$$

$$GHGS < -10 \ (\mathrm{m\ deg.}^{-1}),$$

$$Z_{(\varphi_0,\lambda)} - [Z_{(\varphi_0)}] > 0,$$

where the square brackets denote the zonal mean. Although Kazamoto(2008) adopted *n* = 5, this study sets *n* = 3 because the blocking highs in the Southern Hemisphere tend to persist for shorter durations than those in the Northern Hemisphere (Trenberth and Mo, 1985). As part of this study we found that the distribution of identified blocking highs (c.f.,

Fig. 11) is qualitatively similar for when different *n* values between 1 to 5 were used(not shown). An example of blocking episodes is the case shown in Figs. 2d-f. For this case, an blocking high at about 150°W persisted over four days (from January 17th to January 20th in 1980).

2.6 Modes of internal variability

SAM, Pacific South American mode 1 (PSA1), and PSA2 are defined as the first, second, and third empirical orthogonal functions (EOFs), respectively, for the deseasonalized and area-weighted monthly mean 500hPa geopotential height between 20°S and 70°S (Marshall et al., 2017). We reproduce this by using data for 41 years between 1980 and 2020. with the EOF patterns being shown in Figure S2. Note that PSA1 (PSA2) pattern in this study corresponds to PSA2 (PSA1) in previous studies (Marshall et al., 2017; Shields et al., 2022); the difference is likely due to the difference in analysis period (the contribution rate for EOF2 and EOF3 are 11% and 9% in our case so that they could be easily reversed depending on the analysis period).

3. Results

3.1 *Zonally asymmetric distribution of AR frequency*

Figure 3 shows the distribution of AR detection frequency over the Southern Ocean. Fig. 3 Obviously, the distribution is not zonally symmetric and has a marked geographical dependence. The region with the most detected ARs extends from the southern Atlantic (45°W-0°W, 30°S) south-eastward toward the south-western part of Antarctica (120°W, 80°S), exhibiting a spiral-like structure (see e.g., the contour of 50 $\mathrm{days\ year^{-1}}$). Zhu and Newell (1998), who originally used the AR detection algorithm in this study, suggested that the AR frequency shows a similar distribution to the storm track (See Sec. 4.2 for details).

We find three local maxima with the detection frequency higher than 65 $\mathrm{days\ year^{-1}}$ along this region: the southern Atlantic Ocean (>70 $\mathrm{days\ year^{-1}}$; 45°W-0°W, 30°S), the southern Indian Ocean (>65 $\mathrm{days\ year^{-1}}$; 45°E-90°E, 45°S), and the southern Pacific Ocean (>75 $\mathrm{days\ year^{-1}}$; 150°E-150°W, 60°S). It may be worth mentioning that there is a steep jump between the east and west side of the Drake Passage (60°W, 70°S): the detection frequency is lower in the eastside compared to the west side. For the Antarctic coastal area, the detection frequency is much higher on the west side (>60 $\mathrm{days\ year^{-1}}$) than on the east side (<20 $\mathrm{days\ year^{-1}}$). Also note that over the Antarctic continent, the frequency is high (>20 $\mathrm{days\ year^{-1}}$) for low altitude regions and low (<10 $\mathrm{days\ year^{-1}}$) for high altitude regions. As far as the authors know, such geographical dependency has never been reported in previous studies. Fig. 4

Figure 4a shows the distribution of AR "occurrence" frequency (color). AR occurrence frequency shows a very similar structure to that of the AR detection frequency (Figs. 3 and 4a): the local maxima over the Southern Pacific Ocean and the Indian Ocean agree well between the detection and occurrence frequencies. It should be noted however that the AR occurrence frequencies over the Atlantic and Pacific Oceans are smaller than that over the Indian Ocean (Fig. 4a), while the AR detection frequencies over the Atlantic and Pacific Oceans are larger than that over the Indian Ocean (Fig. 3).

Figure 4b shows the persistence of ARs. The regions where the AR occurrence frequency is greater than 50 year^{-1} and the ARs persist for longer than 1 day are denoted by black contours. It is found that the persistence in the high occurrence frequency region is longer over the Southern Pacific and the Atlantic Ocean (black contour), than the Indian Ocean, which is consistent with the distribution of AR detection frequency and is in the opposite sense for the AR occurrence frequency. These findings suggest that the maxima of AR detection frequency over the Atlantic and the Southern Pacific Oceans (Fig. 3) are attributed to both the occurrence frequency and persistency, while that over the Indian Ocean is mainly to only the occurrence frequency.

Figure 4c shows the number of ARs detection for which only ARs at the first time step in each tracking are considered. The results are thus regarded as the frequency distribution of AR origins. The AR origins are frequently observed on the South American continent, the western Atlantic Ocean, the western Indian Ocean, the eastward of the Drake Passage, and over the Southern Pacific Ocean. The most prominent region of these is the South American continent. In fact, Newell et al. (1992) suggested that this area is the main source of large moisture flux into the Atlantic. Comparing Figs. 3 and 4c, it is found that the AR origins are generally situated on the western side of regions with high AR detection frequency over the western Atlantic and the western Indian Oceans. This seems reasonable considering that typical ARs move eastward on the westerly jet stream. By contrast, over the Southern Pacific Ocean, the local maximum for the AR origin frequency corresponds almost exactly to the that for the AR detection frequency. Such marked difference will be discussed in Sec. 4.2.

3.2 *The role of ARs in moisture transport*

This section examines the contribution of AR to the meridional moisture transport, including its geographical dependence. We calculate the annually accumulated meridional water vapor flux caused by AR (hereafter referred to as "AR-related moisture transport"). Figures 5 compares the AR-related moisture transport (panel a) with the total transport (panel b), with panel c showing their difference. The distribution of AR-related moisture transport (Fig. 5a) aligns closely with the high-frequency region of AR detection (Fig. 3), with local maxima seen over the southward Atlantic, the southward Indian Oceans, and southward of Australia. It is found that these spatial features are also observed in the total moisture transport (Fig. 5b) while the transport caused by other factors than AR is significantly smaller (Fig. 5c).

Fig. 5

A notable difference between Fig. 3 and Fig. 5a may be in that the zonal asymmetry is less evident at high latitudes near the Antarctic continent (poleward of 60°S): Specifically, the AR frequency maximum over the Southern Pacific (Fig. 3) is not so clear in the AR-related moisture transport (Fig. 5a). This is likely due to the fact the moisture content of the air decreases toward the pole (c.f., Fig. 1). However, we still see that a large fraction of moisture transport is caused by AR and that the zonal asymmetry in total moisture transport is largely produced by that in AR activity. (Fig. 5b and 5c; see also Fig. 6 (the lowest panel)).

Fig. 6

Figure 6 shows the zonal variation of meridional moisture transport at 40°, 50°, 60°, and 70°S. It is found that AR (red curves) contributes to up to 70% of the total transport (blue curves). The zonal and meridional dependence of AR-related moisture transport aligns, of course, with the spatial structure as found Fig 5a. At 40°S and 70°S, the AR-related moisture transport is large for the region from 120°E through 180°E/W to 60°W that corresponds to the maximum region for AR detection frequency over the Southern Pacific near Antarctica (Figs. 3 and 5a).

3.3 *Seasonal variations of AR activity and moisture transport*

Fig. 7

Fig. 7 shows the seasonally averaged AR detection frequency. For all seasons, the results are quite similar to the annual-mean (Fig. 3). Among the 4 seasons there are only small differences (from 3% to 6%) within the spiral-like structure.

Fig. 8

Fig. 8a shows the seasonal variations of the total and AR-related moisture transport at 40°, 50°, 60°, and 70°S. The AR-related moisture transport and the total moisture transport show a similar seasonal variation, taking its maximum in austral fall and gradually decreasing toward austral summer at every latitude. This indicates that the seasonal variation of the total moisture transport is also largely explained by that of the AR activity. The contribution rate of AR-related moisture transport to the total one shows little seasonal variation from 40°S to 50°S, while it is large (small) in summer (winter) poleward of 60°S.

To further examine responsible factors for the seasonality in AR-related moisture transport, Figure 8b shows the seasonal variations (3-month running mean) in the individual AR intensity defined from the AR area-averaged IVT (hereafter, the AR intensity; blue lines) and those in the number of AR detection (red lines). The AR intensity has a maximum from austral summer to fall and a minimum in winter, which may reflect the seasonal variation in atmospheric moisture content due to that in temperature via the Clausius-Clapeyron relationship (Fig. 8b). By contrast, the number of AR detections is large from fall through winter to spring, which may be related to the fact that the storm track becomes vigorous in winter due to the strong baroclinic instability below the zonal jet stream that is shifted poleward in this season (Nakamura and Shimpo, 2004). It is seen that these two factors both contribute to the seasonality of AR-related moisture transport.

3.4 The long-term trend of AR activity

Figure 9 shows the time series of seasonal AR intensity values for ARs crossing 60° S together with least squares linear fit over the 41 years analyzed. The results calculated from JRA55 (solid lines) and ERA5 (dashed lines) are presented. It is seen that the two datasets shows a very similar interannual variability and long-term trend including their seasonality. For JRA55, the AR intensity shows a significant positive trend at 99% significant level in DJF (from December to February; 0.63 $\mathrm{kg\,m^{-1}s^{-1}}$) and at 95% significant level in MAM (from March to May; 0.37 $\mathrm{kg\,m^{-1}s^{-1}}$).

Fig. 9

The trend in AR intensity should be explained by the two factors: the trend in the AR area-averaged vertically integrated water vapor (IWV) (Fig. S3) and that in the wind speed in AR. In fact, in DJF, a positive long-term trend of atmospheric temperature has been found over the Southern Ocean (Li and Ding, 2024). Higher temperature should lead to an increase in the atmospheric water vapor content, which leads to larger IWV in AR (Fig. S3), and thus to a positive trend in the AR intensity. in addition, it has been reported that the strengthened polar vortex has led to an increase in surface westerlies at 60°S, recognized as the poleward shift of surface westerlies or a positive trend in the SAM index (Chen and Held, 2017). Indeed, Li and Ding (2024) suggested that AR frequency (detected using a temporally fixed threshold though) increased around 60°S over the Southern Ocean for the last four decades due to the poleward shift of AR; this trend likely corresponds to the positive trend in the AR intensity in the present case. It may be worth mentioning that while the long-term trends of AR intensity are similar between JRA55 and ERA5, there is a marked difference in the IWV trend between the two datasets (Figs. 9 and S3). This indicates that the relative importance of the two factors (i.e., IWV or wind speed) for the AR intensity trend is slightly different between the two datasets. In MAM, albeit a similar trend in the IWV, its magnitude was reported to be relatively small compared to those in DJF (Marshall, 2003) (see also Fig. S3), consistent with the trend in AR intensity found in this study.

For JJA (from June to August) and SON (from September to November), by contrast, the AR intensity shows a relatively weak positive trend (0.15 $\mathrm{kg\,m^{-1}s^{-1}}$ in JJA (no significant level) and that of 0.24 $\mathrm{kg\,m^{-1}s^{-1}}$ in SON (no significant level)) compared to that in DJF and MAM. Such seasonal contrast may be associated with the seasonality of the

Antarctic sea ice extent. The Antarctic sea ice extent takes its maximum in September and it often reaches 60°S in austral winter (JJA and SON) (Parkinson and Cavalieri, 2012; Turner et al., 2015). Francis et al. (2020) suggested that the water vapor capacity of a cold atmosphere, and thus IVT, rapidly decreases over the sea ice zone. At least for the satellite observation era (since1979), the Antarctic sea ice extent has been increasing (especially in the Ross sea sector, where the AR detection frequency takes its maximum at 60°S) (Parkinson and Cavalieri, 2012; Turner et al., 2015). This factor may account for the negligible trend in the AR intensity during austral winter.

Figure 10 shows the time series of seasonal AR detection number for ARs that cross 60°. By contrast to the long term trend of AR intensity (Fig. 9), that of the AR detection number has no significant trends in any season for both JRA55 and ERA5 (Fig. 10). As noted in Introduction, some previous studies using the climatological threshold for the AR detection algorithm showed a climatologically positive trend in AR detection frequency (e.g., Wille et al., 2019). This study instead shows that the AR detection number does not change, while the individual AR intensity shows an increasing trend (again for DJF and MAM; Fig. 9). Newell et al. (1992) have reported that there are typically five ARs at one time over the Southern Ocean in mid-latitudes. Our finding suggests that the number of ARs over the Southern Ocean is still typically five, while their individual intensity has been strengthening.

4. Discussion

4.1 Comparison with previous studies

As noted in the Introduction, recent studies reported that the AR frequency and the resultant climatological meridional moisture flux basically had a zonally symmetric distribution (Guan and Waliser, 2015, 2023; Nash et al., 2018; Wille et al., 2021). Our study, by contrast, has clearly demonstrated that the AR detection frequency has a zonally asymmetric distribution. Such disagreement is likely caused by the difference in the AR detection algorithms. As noted in Section 2.2., most previous studies applied an algorithm that used a temporally fixed but spatially dependent, criteria for AR detection (i.e., a percentile value for IVT at each grid point) so that the geographical distribution was hardly produced: in Appendix A, we present further discussion by revisiting the algorithm proposed by Wille et al. (2021). The present study instead adopts the algorithm originally proposed by Zhu and Newell (1998) that searches for an area that has anomalous IVT at each time step. This is suitable for detecting “rivers” as visualized by the IVT and also for examining the geographical distribution because the criteria for detection do not depend on local climatology. Notably, this zonally asymmetric feature is consistent with the distribution of the annual total precipitation over Antarctica (Bromwich et al., 2004): the AR activity and the resultant moisture transport is stronger in the western hemisphere along the Antarctic coastal region.

The contribution of ARs to total moisture transport (about 70%) is smaller than that reported in previous studies. Zhu and Newell (1998) reported that the AR’s contribution is ~90% even though their algorithm was adopted in the present study. Nash et al. (2018) also suggested that the contribution is ~90% while they used the AR algorithm developed by Guan and Waliser (2015), which regarded the area with the IVT larger than its 85th percentile as IVT. The difference between the present and these two previous studies may result from the fact that we set the geometric requirements and the lower limit for IVT in the algorithm (see details in Sec. 2.2). Although there is such a difference in the AR contribution fraction, the seasonal variation of AR contribution to the total transport, i.e., maximum in summer, is qualitatively consistent with that reported in a previous study (Zhu and Newell,1998).

4.2 Synoptic-scale phenomena contributing to the AR activity

This section discusses two meteorological factors namely, storm track and blocking high, to interpret the geographical distribution in AR frequency. These factors were thought to be keys for AR occurrence (e.g., Zhu and Newell, 1998; Wille et al., 2021) but their relative roles have not been examined in detail. In Sec. 3 we highlighted the presence of three distinct maxima in the AR detection frequency: the southern Atlantic Ocean, the southern Indian Ocean, and the southern Pacific Ocean. Recalling that the AR occurrence frequency is mainly responsible for the maximum in the Indian Ocean, while the persistence as well as the occurrence frequency are both responsible for the maxima in the Atlantic and in the southern Pacific Ocean, we infer that responsible factors are different depending on the geographical location.

a. Indian Ocean

Fig. 11

Figure 11a shows the horizontal distributions of annual-mean synoptic-scale EKE as an indicator of the storm track axis. EKE is relatively strong in the eastern hemisphere and takes its maximum in the south-eastern Indian Ocean. According to Inatsu and Hoskins (2004), the geographical dependence of the storm track can be attributed to the orography of the Andes and the South African Plateau and the midlatitude sea surface temperature anomaly.

Notably, this maximum region of EKE agrees well with the maximum of AR detection frequency over the Indian Ocean. It is thus likely that the AR origins in this region are mostly associated with eastward-traveling extratropical cyclones that are born in the western part of the Indian Ocean (~40°E, c.f., Fig. 4c) and reach their mature stage at ~90°E (Figure 11a). The AR appearing in Figs. 2a-c is regarded as an example of this type. We see that it is moving eastward toward the Indian Ocean while developing.

Fig. 12

To further support this conclusion, Figure 12 shows the composite mean of geopotential height (GPH) anomalies at 500 hPa level from the annual-mean climatology. The composite is taken for the cases when ARs touched the area with AR detection frequency larger than 65 $\mathrm{days\ year^{-1}}$ over the Indian Ocean (the ARs detection frequency for this case is denoted by the green contours). It is observed that a typical AR in this region accompanies a negative and positive GPH anomaly on its west and east, respectively (Fig. 12a), suggesting again that the AR activity in this region is often associated with extratropical cyclones.

b. Atlantic Ocean

The maximum of AR detection/occurrence over the Atlantic Ocean (Figs 3 and 4a) also seems to correspond to some part of the storm track, but the EKE is relatively low compared to that over the Indian Ocean. The composite mean GPH anomaly over the Atlantic Ocean is shown in Fig. 12b. This composite is taken for the cases when ARs touched the area with AR detection frequency larger than 70 $\mathrm{days\,year}^{-1}$. We see that the geopotential pattern is qualitatively similar to that over the Indian Ocean (Figs. 12a and 12b), but these anomalies are smaller than those in the Indian Ocean as is consistent with the lower EKE.

We here note again that the persistence is long for this region (Fig. 4b) and that there is a maximum region for the number of AR origins over the South American continent (Fig. 4c). Newell et al. (1992) suggested that ARs were often born over the Amazon and that they travel southeastward into the Atlantic. On the South American continent, the northerly wind originating from the tropics holds significant moisture and is present throughout the year (James and Anderson, 1984).

It may be thus speculated that the maximum AR detection frequency over the Atlantic is related to the quasi-stationary moisture transport by the northerly wind at the western edge of the subtropical high over the Atlantic, and that these ARs are related to the genesis and/or early-stage development of the extratropical cyclones.

c. Pacific Ocean

Figure 11b shows the horizontal distribution of the blocking high frequency in the Southern Hemisphere. The geographical dependence agrees with that reported in a previous study (Trenberth and Mo, 1985) in that blocking highs frequently occur in the western South Pacific Ocean. We clearly see that this maximum region corresponds well to the local maxima of the number of AR occurrences (Fig. 4a), the number of AR origins (Fig. 4c), and persistence of ARs in this region (Fig. 4b). It is indicated that the blocking events not only prevent ARs from moving eastward and make them persist in this area but also contribute to the generation of new ARs in this region (Fig. 4c). The AR appearing in Figs. 2d-f is regarded as an example of this type. We see that humid air is intruding into the Antarctica along the western edge of the blocking high, which persists (at least) over the three consecutive days.

The importance of the blocking is also supported by the composite of GPH anomaly distribution in this region (Fig. 12c). This composite is taken for the cases when ARs touched the area with AR detection frequency larger than 75 $days\ year^{-1}$. A typical AR in this region accompanies a positive GPH anomaly, showing a quite different feature from the composite in other regions (Fig. 12). The AR detection frequency shows its maximum downstream of the IVT along the anomalous high, indicating that the blocking high is mainly responsible for the AR over the Southern Pacific Ocean.

It was suggested that a favorable environment for the blocking in the western South Pacific is associated with the planetary wave with zonal wave number 1 (Trenberth and Mo, 1985). Van Loon and Jenne (1972) indicated that the planetary wave itself is forced by the zonally asymmetric topography of the Antarctic continent. Thus, the Antarctic topography may indirectly contribute to making ARs form and persist in the South Pacific Ocean.

4.3 Interannual variability in AR detection number

As discussed in previous studies (Wille et al., 2021; Shields et al., 2022), the interannual variability in the appearance of AR may be associated with the atmospheric interannual variability, such as the SAM and PSA1 patterns. It is known that the SAM and PSA1 patterns are associated with the wind circulation and moisture transport around Antarctica, especially around west Antarctica (Marshall et al., 2017). Notably, the geopotential patterns for these modes (Fig. S2) show a positive anomaly over the Pacific sector that is similar to the composite pattern for the cases of AR appearing in this region. (Fig. 12c).

Actually, we find that the time series of the deseasonalized monthly cumulative AR number composited in the Pacific sector (AR time series) is correlated with both time series of SAM and PSA1, with correlation coefficients of 0.42 and 0.35, respectively (Figs. S4a and S5a). The coefficient of determination (R^2) obtained from the multiple linear regression analysis between the AR time series and the time series of SAM and PSA is 0.30 (that obtained from simple linear regression analysis is 0.18 and 0.12, respectively.)

The interannual variability of the maxima AR detection frequency in other sectors is also compared to the time series of the SAM index, but the correlation coefficients are found insignificant, -0.15 and 0.02 over the Atlantic and the Indian Ocean, respectively (Figs. S4b and S4c).

5. Conclusion

This study comprehensively examined the morphology of AR in the south polar region using an AR detection method that extracts localized, narrow IVT area at each time step. This method contracts with conventional methods which use some fixed, percentile value defined at each grid point for AR detection. These earlier approaches lead to detection numbers tending to be the same at all grids (i.e., zonally symmetric): also more ARs tend to be detected in more recent years due to the increase in background water vapor content.

With the present method, we discovered that the AR frequency distribution shows a zonally asymmetric, spiral-like structure from the Atlantic at mid-laltitudes to the Southern Pacific at high latitudes, with three distinct maxima in the Atlantic, Indian, and Pacific Oceans. Such a geographical dependence has not been reported in previous studies.

The ARs play a significant role in meridional moisture transport, accounting for 70% of total transport. The moisture transport also has a clear zonal asymmetry which we find can be explained by the zonal asymmetric distribution of AR. This finding may in turn explain some part of the geographical dependence of precipitation over the Antarctic continent. The AR-related moisture transport shows a seasonal variation being large from austral fall through winter to spring. This seasonal variation is attributed both to the number of ARs (maximum from fall to winter) and the individual AR intensity (maximum from summer to fall).

We further discussed the meteorological factors contributing to the local maxima of the AR detection frequency. The ARs over the Indian Ocean and the Atlantic are likely associated with extratropical cyclones but with a slight difference: those over the Indian Ocean are likely associated with developed, eastward moving cyclones, while those over the Atlantic are likely formed along quasi-stationary, northerly wind from the South American continent and are associated with developing cyclones. By contrast, ARs over the Southern Pacific are primarily attributed to blocking highs. Notably, these results are consistent with the analysis of AR tracking that enabled us to examine the horizontal distribution of the origin and persistence of ARs. We find that the number of AR detections has a marked interannual variability. Especially, the variability over the Southern Pacific are in part correlated with the SAM and PSA, as their mode structures in geopotential height are similar to the pattern for the cases of AR appearing in this region.

It is also found that the AR intensity (the mean IVT in one AR) shows a positive long-term trend in DJF and MAM, while there was no significant trend in the AR detection number. We discussed that the reason for the small trends in austral winter may be related to the increasing trend of sea ice extent and the resultant decrease in IVT over the sea ice zone According to recent study, however, Antarctic sea ice extent has started to decrease rapidly since 2016 (Purich and Doddridge, 2023). This may cause the intensification of individual ARs even in austral winter. Furthermore, intense ARs can contribute to the formation of

Antarctic sea ice polynya and maintain it from austral winter to spring (Francis et al., 2020). To understand such an interaction between ARs and sea ice, the long-term trend of ARs need to be further examined.

Recently an increasing trend in the annual snow accumulation rate has been reported at several places over Antarctica (e.g., Wang et al., 2021; Oyabu et al., 2023). Considering that the AR is reported to contribute to snow accumulation over inland Antarctica (Gorodetskaya et al., 2014; Wille et al., 2021, 2024), the observed trend in surface mass balance may be in part explained by the positive trend of AR activity discovered in this study. However, it was suggested that the AR had also a negative impact on the ice mass due to the calving of ice shelves (Bozkurt et al., 2018; Wille et al., 2019, 2022). Thus, further analysis is necessary for quantifying the two counter effects in a future study.

Data Availability Statement

The JRA55 dataset was collected and distributed by Research Institute for Sustainable Humanosphere, Kyoto University (http://database.rish.kyoto-u.ac.jp/index-e.html). ERA5 data is available from the Copernicus Climate Change Service (C3S) Climate Data Store at (https://doi.org/10.24381/cds.adbb2d47). The code will be provided upon request.

Appendix

A. Comparison with the *AR detection algorithm developed by Wille et al. (2021)*

Many recent studies use temporally fixed, spatially dependent criteria for AR detection. In this Appendix, we discuss how the results obtained with such a conventional approach differ from the present results. Here, we trace the algorithm utilized by Wille et al. (2021) (hereafter referred to as the "W-method"), who showed that the resultant AR frequency distribution was zonally symmetric over the south polar region.

The W-method considers the domain between 37.5°S and 80°S, and the objects within this domain that satisfy the following two conditions are regarded as ARs: (1) the meridional component of IVT exceeds the 98th percentile value at each grid point, and (2) they extend at least 20°S in the meridional direction.

Figure A1 shows the annual mean AR frequency as reproduced with the W-method using JRA55 data. The distribution is zonally-symmetric, with its maxima being located around 60°S. This is consistent with the results of Wille et al. (2021) (see their Fig. 2), who used ERA-5 data for the period between 1980 and 2018. The distribution has a marked contrast with the present result (Fig.3), which shows a clear zonally asymmetric distribution.

The zonally symmetric distribution in AR frequency from the W-method is understandable since the frequency is automatically limited by 2% (recall the vIVT condition (1) above). Note that the frequency is not exactly equal but slightly smaller than 2% because of the condition (2): even if a high vIVT object satisfies the condition (1), it is hard to meet the condition (2) near the meridional boundary of the analysis domain (37.5°S or 80°S). This is demonstrated in Figure A2, which shows how the two different methods (the present method (green contours) and the W-method (purple solid contours)) detect ARs on 7th and 8th May 2019 (these are identical to the cases in Figs. 2b and 2c). Additionally, for the W-method, the objects meeting IVT threshold but not geometric criteria are represented as the dashed purple contours. Both methods basically detect the same objects, but for the W-method, the geometric criteria and the meridional boundary inhibit them from being identified as ARs. For example, a high-IVT object located in the center of the panel of Fig. A2 shows a meridionally elongated structure (green solid contour), but the boundary at 37.5S artificially cut the object, and its meridional extension is underestimated (purple dashed contour).

B. *Sensitivity to AR detection parameter and the necessity of geometric condition for the present study*

Figure B1 shows the AR detection frequency with the IVT threshold changed from 30% of the maximum zonal anomaly (default value) to 20% (Fig. B1a) or 40% (Fig. A3b). In either case, the AR detection frequencies are qualitatively similar in distribution with the case with 30% (Fig. 3). This indicates that the zonally asymmetric distribution of AR detection frequency is a robust feature.

By contrast, the geometric criteria play a key role in AR detection especially near south pole. Figure B2 shows the AR frequency distribution as deduced without geometric criteria applied. Comparing this with Fig. 3 (with geometric criteria applied), we see that the results change little over the ocean, while there are significant differences at higher latitudes especially over the continent (>60°S): the frequency over west Antarctica is much higher in Fig. B2 than Fig. 3. This is likely due to the fact that the IVT is climatologically high in this region so that this area is sometimes regarded as AR even if it does not have a long-shaped, river-like structure with moisture transport from lower latitudes. To avoid detecting such relatively high IVT areas involving no moisture transport from lower latitudes, the geometric requirement needs to be applied to identify the AR detection frequency distribution.

Supplement

Figure S1 shows the annual-mean AR frequency as derived from the ERA5 dataset. Figure S2 shows the spatial patterns of the first, second, and third EOF (empirical orthogonal function) in geopotential height at 500 hPa, which represents the spatial patterns of SAM, PSA1, and PSA2 respectively. Figure S3 shows the seasonal mean vertically integrated water vapor anomalies from the 41-year mean of ARs crossing 60°S between 1980 and 2020 and its linear trend as derived from JRA55 and ERA5.

Acknowledgments

This work was in part supported by JST, the establishment of university fellowships towards the creation of science technology innovation (Grant Number: JPMJFS2136) and in part by JSPS KAKENHI Grant Number 21K03661 and 24K00706. We are greatly thankful to the late Masato Shiotani and Kenshi Takahashi who provided helpful comments about this study and led the laboratory in which that the first author worked during his master course. We are also thankful to Kevin Hamilton and three anonymous reviewers for their valuable comments which helped to greatly improve the manuscript.

References

Baiman, R., A. C. Winters, B. Pohl, V. Favier, J. D. Wille, and K. R. Clem, 2024: Synoptic and planetary-scale dynamics modulate antarctic atmospheric river precipitation intensity. *Communications Earth & Environment*, *5*(1), 127.

Barriopedro, D., R. García-Herrera, A. R. Lupo, and E. Hernández, 2006: A Climatology of Northern Hemisphere Blocking. *J. Clim.* **19**, 1042–1063.

Bozkurt, D., R. Rondanelli, J. C. Marín, and R. Garreaud, 2018: Foehn Event Triggered by an Atmospheric River Underlies Record-Setting Temperature Along Continental Antarctica. *J. Geophys. Res. Atmospheres* **123**, 3871–3892.

Bromwich, D. H., Z. Guo, L. Bai, and Q. -S. Chen, 2004: Modeled Antarctic Precipitation. Part I: Spatial and Temporal Variability. *J. Clim.* **17**, 427–447.

Chemke, R., 2022: The future poleward shift of Southern Hemisphere summer mid-latitude storm tracks stems from ocean coupling. *Nature communications*, *13*(1), p.1730.

Chen, G. and I.M. Held, 2007: Phase speed spectra and the recent poleward shift of Southern Hemisphere surface westerlies. *Geophysical Research Letters*, *34*(21).

Church, J. A. and J. M. Gregory, 2001: *Changes in sea level*, Cambridge University Press, 641-693 pp.

Francis, D., C. Eayrs, J. Cuesta, and D. Holland, 2019: Polar cyclones at the origin of the reoccurrence of the Maud Rise Polynya in austral winter 2017. *J. Geophys. Res. Atmospheres*, 124, 5251–5267.

Francis, D., K.S. Mattingly, M. Temimi, R. Massom, and P. Heil, 2020: On the crucial role of atmospheric rivers in the two major Weddell Polynya events in 1973 and 2017 in Antarctica. *Science advances*, *6*(46), eabc2695.

Fujita, K., and O. Abe, 2006: Stable isotopes in daily precipitation at Dome Fuji, East Antarctica. *Geophys. Res. Lett.* **33**.

Gorodetskaya, I. V., M. Tsukernik, K. Claes, M. F. Ralph, W. D. Neff, and N. P. M. van Lipzig, 2014: The role of atmospheric rivers in anomalous snow accumulation in East Antarctica. *Geophys. Res. Lett.* **41**, 6199–6206.

Gehring, J., É. Vignon, A. C. Billault-Roux, A. Ferrone, A. Protat, S. P. Alexander, and A. Berne, 2022: Orographic flow influence on precipitation during an atmospheric river event at Davis, Antarctica. *Journal of Geophysical Research: Atmospheres*, *127*(2), e2021JD035210.

Gonzales, K. R., D. L. Swain, K. M. Nardi, E. A. Barnes, and N. S. Diffenbaugh, 2019: Recent warming of landfalling atmospheric rivers along the west coast of the United States. *Journal of Geophysical Research: Atmospheres*, *124*(13), 6810-6826.

Guan, B. and D. E. Waliser, 2015: Detection of atmospheric rivers: Evaluation and application of an algorithm for global studies. *J. Geophys. Res. Atmospheres* **120**, 12514–

12535.

Guan, B., and D. E. Waliser, 2019: Tracking Atmospheric Rivers Globally: Spatial Distributions and Temporal Evolution of Life Cycle Characteristics. *J. Geophys. Res. Atmospheres* **124**, 12,523–12,552.

Guan, B., D. E. Waliser, and F. M. Ralph, 2023: Global application of the atmospheric river scale. *Journal of Geophysical Research: Atmospheres*, *128*(3), e2022JD037180.

Hersbach, H., B. Bell, P. Berrisford, S. Hirahara, A. Horányi, J. Muñoz-Sabater, J. Nicolas, C. Peubey, R. Radu, D. Schepers, A. Simmons, C. Soci, S. Adballa, X. Abellan, G. Balsamo, P. Bechtold, G. Biavati, J. Bidlot, M. Bonavita, G. D. Chiara, P. Dahlgren, D. Dee, M. Diamantakis, R. Dragani, J. Flemming, R. Forbes, M. Fuentes, A. Geer, L. Haimberger, S. Healy, R. J. Hogan, E. Hólm, M. Janisková, S. Keeley, P. Laloyaux, P. Lopez, C. Lupu, G. Radnoti, P. D. Rosnay, I. Rozum, F. Vamborg, S. Villaume, and J. -N. Thépaut, 2020: The ERA5 global reanalysis. *Quarterly Journal of the Royal Meteorological Society*, **146**(730), 1999–2049.

Hirasawa, N., H. Nakamura, and T. Yamanouchi, 2000: Abrupt changes in meteorological conditions observed at an inland Antarctic Station in association with wintertime blocking. *Geophys. Res. Lett.* **27**, 1911–1914.

Inatsu, M. and B. J. Hoskins, 2004: The Zonal Asymmetry of the Southern Hemisphere Winter Storm Track. *J. Clim.* **17**, 4882–4892.

Kamae, Y., W. Mei, S.-P. Xie, M. Naoi, H. Ueda, 2017: Atmospheric Rivers over the

Northwestern Pacific: Climatology and Interannual Variability. *J. Clim.* **30**, 5605–5619.

Kazamoto, K., 2008: Analytical Study of Relationship between Blocking and Sudden Warming. master thesis, Graduate school of Science, Kyoto University.

Kobayashi, S., Y. Ota, Y. Harada, A. Ebita, M. Morita, H. Onoda, K. Onogi, H. Kamahori, C. Kobayashi, H. Endo, K. Miyaoka, and K. Takahashi, 2015: The JRA-55 Reanalysis: General Specifications and Basic Characteristics. *J. Meteorol. Soc. Jpn. Ser II* **93**, 5–48.

Li, Z., and Q. Ding, 2024: A global poleward shift of atmospheric rivers. *Science Advances*, *10*(41), eadq0604.

Maclennan, M. L., J. T. M. Lenaerts, C. Shields, and J. D. Wille, 2022: Contribution of Atmospheric Rivers to Antarctic Precipitation. *Geophys. Res. Lett.* **49**, e2022GL100585.

Marshall, G.J., 2003. Trends in the Southern Annular Mode from observations and reanalyses. *J. Clim. 16*(24), pp.4134-4143.

Marshall, G. J., Thompson, D. W., and van den Broeke, M. R. 2017: The signature of Southern Hemisphere atmospheric circulation patterns in Antarctic precipitation. *Geophys. Res. Lett. 44*(22), 11-580.

Mundhenk, B. D., E. A. Barnes, and E. D. Maloney, 2016: All-Season Climatology and Variability of Atmospheric River Frequencies over the North Pacific. *J. Clim.* **29**, 4885–4903.

Nakamura, H. and A. Shimpo, 2004: A. Seasonal Variations in the Southern Hemisphere Storm Tracks and Jet Streams as Revealed in a Reanalysis Dataset. *J. Clim.* **17**, 1828–

1844.

Nash, D., D. Waliser, B. Guan, H. Ye, and F. M. Ralph, 2018: The Role of Atmospheric Rivers in Extratropical and Polar Hydroclimate. *J. Geophys. Res. Atmospheres* **123**, 6804–6821.

Neiman, P. J., L. J. Schick, F. M. Ralph, M. Hughes, and G. A. Wick, 2011: Flooding in Western Washington: The Connection to Atmospheric Rivers. *J. Hydrometeorol.* **12**, 1337–1358.

Newell, R. E., N. E. Newell, Y. Zhu, and C. Scott, 1992: Tropospheric rivers? – A pilot study. *Geophys. Res. Lett.* **19**, 2401–2404.

Oyabu, I., Kawamura, K., Fujita, S., Inoue, R., Motoyama, H., Fukui, K., ... & Yoshimori, M. 2023: Temporal variations of surface mass balance over the last 5000 years around Dome Fuji, Dronning Maud Land, East Antarctica. *Climate of the Past*, *19*(2), 293-321.

Parkinson, C. L., and D. J. Cavalieri, 2012. Antarctic sea ice variability and trends, 1979–2010. *The Cryosphere*, *6*(4), 871-880.

Payne, A. E., and G. Magnusdottir, 2014: Dynamics of landfalling atmospheric rivers over the North Pacific in 30 years of MERRA reanalysis. *Journal of Climate*, *27*(18), 7133-7150.

Purich, A., and E. W. Doddridge, 2023. Record low Antarctic sea ice coverage indicates a new sea ice state. *Communications Earth & Environment*, *4*(1), 314.

Ralph, F. M. and M. D. Dettinger, 2011: Storms, floods, and the science of atmospheric rivers. *Eos Trans. Am. Geophys. Union* **92**, 265–266.

Ralph, F. M., M. Dettinger, D. Lavers, I. V. Gorodetskaya, A. Martin, M. Viale, A. B. White, N. Oakley, J. Rutz, J. R. Spackman, H. Wernli, and J. Cordeira, 2017a: Atmospheric Rivers Emerge as a Global Science and Applications Focus. *Bull. Am. Meteorol. Soc.* **98**, 1969–1973.

Ralph, F. M., S. F. Iacomellis, P. J. Neiman, J. M. Cordeira, J. R. Spackman, D. E. Waliser, G. A. Wick, A. B. White, and C. Fairall, 2017b: Dropsonde Observations of Total Integrated Water Vapor Transport within North Pacific Atmospheric Rivers. *J. Hydrometeorol.* **18**, 2577–2596.

Ralph, F. M., P. J. Neiman, and G. A. Wick, 2004: Satellite and CALJET Aircraft Observations of Atmospheric Rivers over the Eastern North Pacific Ocean during the Winter of 1997/98. *Mon. Weather Rev.* **132**, 1721–1745.

Rutz, J. J., C. A. Shields, J. M. Lora, A. E. Payne, B. Guan, P. Ullrich, T. O'Brien, L. R. Leung, F. M. Ralph, M. Wehner, S. Brands, A. Collow, N. Goldenson, I. Gorodetskaya, H. Griffith, K. Kashinath, B. Kawzenuk, H. Krishnan, V. Kurlin, D. Lavers, G. Magnusdottir, K. Mahoney, E. McClenny, G. Muszynski, P. D. Nguyen, Mr. Prabhat, Y. Qian, A. M. Ramos, C.Sarangi, S.Sellars, T. Shulgina, R. Tome, D. Waliser, D. Walton, G. Wick, A. M. Wilson, and M. Viale, 2019: The Atmospheric River Tracking Method Intercomparison Project (ARTMIP): Quantifying Uncertainties in Atmospheric River Climatology. *J. Geophys. Res. Atmospheres* **124**, 13777–13802.

Shepherd, A. and D. Wingham, 2007: Recent Sea-Level Contributions of the Antarctic and

Greenland Ice Sheets. *Science* **315**, 1529–1532.

Shields, C. A., J.J. Rutz, L. -Y. Leung, F. M. Ralph, M. Wehner, B. Kawzenuk, J. M. Lora, E. McClenny, T. Osborne, A. E. Payne, P. Ullrich, A. Gershunov, N. Goldenson, B. Guan, Y. Qian, A. M. Ramos, C. Sarangi, S. Sellars, I. Gorodetskaya, K. Kashinath, V. Kurlin, K. Mahoney, G. Muszynski, R. Pierce, A. C. Subramanian, R. Tome, D. Waliser, D. Walton, G. Wick, A. Wilson, D. Lavers, Prabhat, A. Collow, H. Krishnan, G. Magnusdottir, and P. Nguyen, 2018: Atmospheric River Tracking Method Intercomparison Project (ARTMIP): project goals and experimental design. *Geosci. Model Dev.* **11**, 2455–2474.

Sinclair, V. A. and H. F. Dacre, 2019: Which Extratropical Cyclones Contribute Most to the Transport of Moisture in the Southern Hemisphere? *J. Geophys. Res. Atmospheres* **124**, 2525–2545.

Terpstra, A., I. V. Gorodetskaya, and H. Sodemann, 2021: Linking sub-tropical evaporation and extreme precipitation over East Antarctica: An atmospheric river case study. *Journal of Geophysical Research: Atmospheres*, *126*(9), e2020JD033617.

Thompson, D.W. and S. Solomon, 2002: Interpretation of recent Southern Hemisphere climate change. *Science*, *296*(5569), pp.895-899.

Trenberth, K. F. and K. C. Mo, 1985: Blocking in the Southern Hemisphere. *Mon. Weather Rev.* **113**, 3–21.

Turner, J., J. S. Hosking, T. J. Bracegirdle, G. J. Marshall, and T. Phillips, 2015. Recent changes in Antarctic sea ice. *Philosophical Transactions of the Royal Society A:*

Mathematical, Physical and Engineering Sciences, *373*(2045), 20140163.

Turner, J., T. Phillips, M. Thamban, W. Rahaman, G. J. Marshall, J. D. Wille, V. Favier, V. H. L. Winton, E. Thomas, Z. Wang, M. van den Broeke, J. S. Hosking, and T. Lachlan-Cope, 2019: The Dominant Role of Extreme Precipitation Events in Antarctic Snowfall Variability. *Geophys. Res. Lett.* **46**, 3502–3511.

Vaughan, D. G., J. L. Bamber, M. Giovinetto, J. Russell, and A. P. R. Cooper, 1999: Reassessment of Net Surface Mass Balance in Antarctica. *J. Clim.* 12, 933–946.

Wang, L., J. L. Davis, and I. M. Howat, 2021: Complex Patterns of Antarctic Ice Sheet Mass Change Resolved by Time-Dependent Rate Modeling of GRACE and GRACE Follow-On Observations. *Geophysical Research Letters*, *48*(1), e2020GL090961.

Wille, J. D., V. Favier, A. Dufour, I. Gorodetskaya, J. Turner, C. Agosta, and F. Codron, 2019: West Antarctic surface melt triggered by atmospheric rivers. *Nat. Geosci.* **12**, 911–916.

Wille, J. D., V. Favier, I. V. Gorodetskaya, C. Agosta, C. Kittel, J. C. Beeman, N. C. Jourdain, J. T. M. Lenaerts, and F. Codron, 2021: Antarctic Atmospheric River Climatology and Precipitation Impacts. *J. Geophys. Res. Atmospheres* **126**, e2020JD033788 (2021).

Wille, J. D., V. Favier, N. C. Jourdain, C. Kittel, J. V. Turton, C. Agosta, I. V. Gorodetskaya, G. Picard, F. Codron, C. L. -D. Santos, C. Amory, X. Fettweis, J. Blanchet, V. Jomelli, and A. Berchet, 2022: Intense atmospheric rivers can weaken ice shelf stability at the Antarctic Peninsula. *Commun. Earth Environ.* **3**, 1–14.

Wille, J. D., S. P. Alexander, C. Amory,R. Baiman, L. Barthélemy, D. M. Bergstrom, A. Berne, H. Binder, J. Blanchet, D. Bozkurt, T. J. Bracegirdle, M. Casado, T. Choi, K. R. Clem, F. Codron, R. Datta, R. D. Garreaud, C. Genthon, I. V. Gorodetskaya, S. González-Herrero, V. J. Heinrich, G. Hubert, H. Joos, S.-J. Kim, J. C. King, C. Kittle, A. Landais, M. Lazzara, G. H. Leonard, J. L. Lieser, M. Maclennan, D. Mikolajczyk, P. Neff, I. Ollivier, G. Picard, B. Pohl, F. M. Ralph, P. Rowe, E. Schlosser, C. A. Shields, I. J. Smith, M. Sprenger, L. Trusel, D. Udy, T. Vance, É. Vignon, C. Walker, N. Wever, and X. Zou, 2024: The extraordinary March 2022 East Antarctica “heat” wave. Part II: impacts on the Antarctic ice sheet. *Journal of Climate*, *37*(3), 779-799.

Wille, J. D., B. Pohl, V. Favier, A. C. Winters, R. Baiman, S. M. Cavallo, C. L.-D. Santos, K. Clem, D. G. Udy, T. R. Vance, I. Gorodetskaya, F. Codron, and A. Berchet, 2024b: Examining atmospheric river life cycles in East Antarctica. *J. Geophys. Res. Atmospheres* ***129***(8), e2023JD039970.

Wingham D. J., A. Shepherd, A. Muir, and G. J. Marshall, 2006: Mass balance of the Antarctic ice sheet. *Phil. Trans. R. Soc. A.***364**, 1627–1635.

Zhang, Z., F. M. Ralph, and M. Zheng, 2019: The relationship between extratropical cyclone strength and atmospheric river intensity and position. *Geophys. Res. Lett.* **46**(3), 1814-1823.

Zhou, Y., H. Kim, and B. Guan, 2018: Life cycle of atmospheric rivers: Identification and climatological characteristics. *Journal of Geophysical Research: Atmospheres*, *123*(22), 12-715.

Zhu, Y. and R. E. Newell, 1994: Atmospheric rivers and bombs. *Geophys. Res. Lett.* **21**, 1999–2002.

Zhu, Y. and R. E. Newell, 1998: A Proposed Algorithm for Moisture Fluxes from Atmospheric Rivers. *Mon. Weather Rev.* **126**, 725–735.

List of Figures

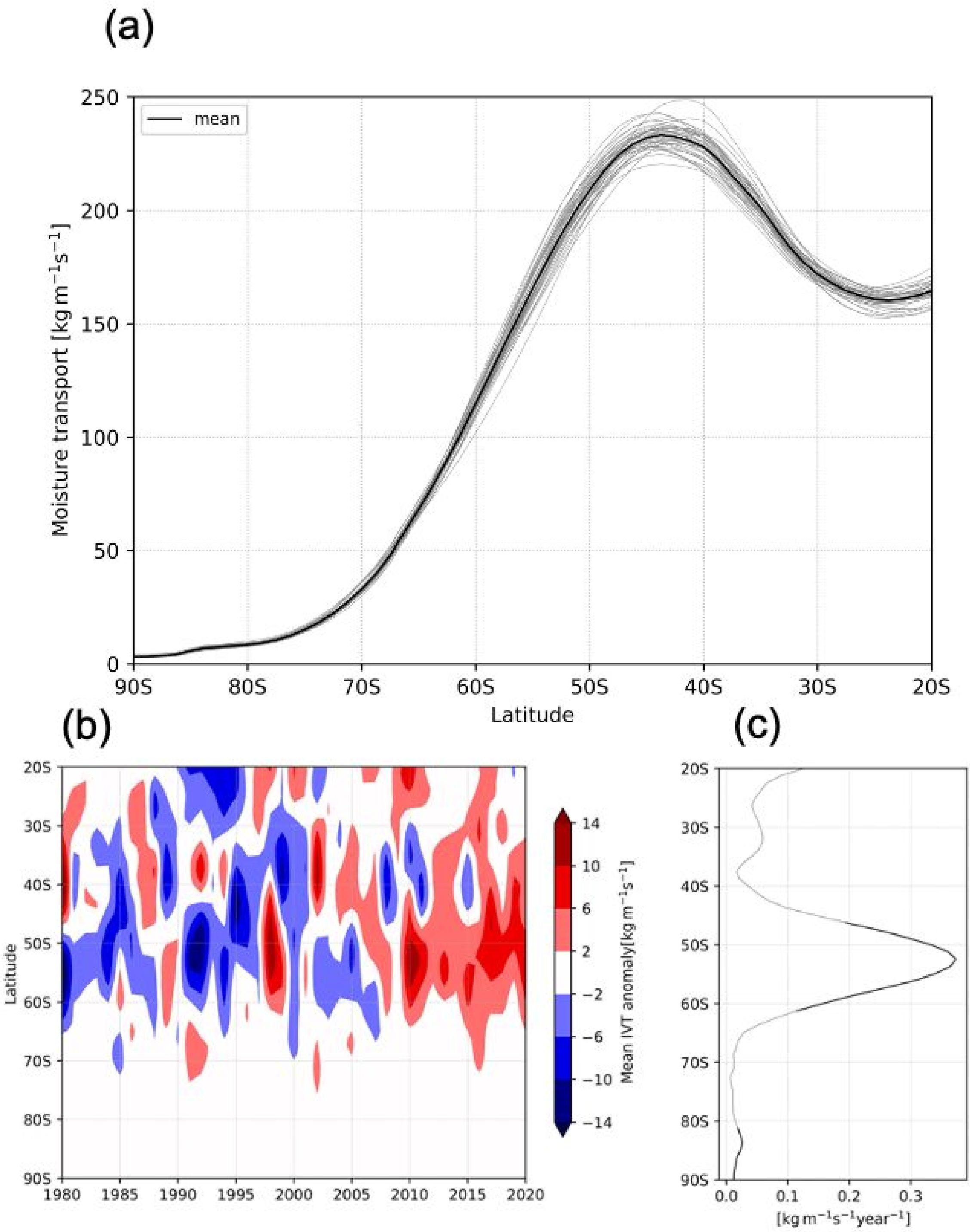

Fig. 1 (a) The latitudinal distribution of (black curve) zonal-mean IVT averaged over 1980-2020 and (gray curves) that for individual years. (b) The time-latitude section of the anomaly of zonal mean IVT from the average over the 41-years. (c) The climatological trend of zonal mean IVT. Black curves indicates a 99% significant level while gray curve indicates that the trend is not statistically significant.

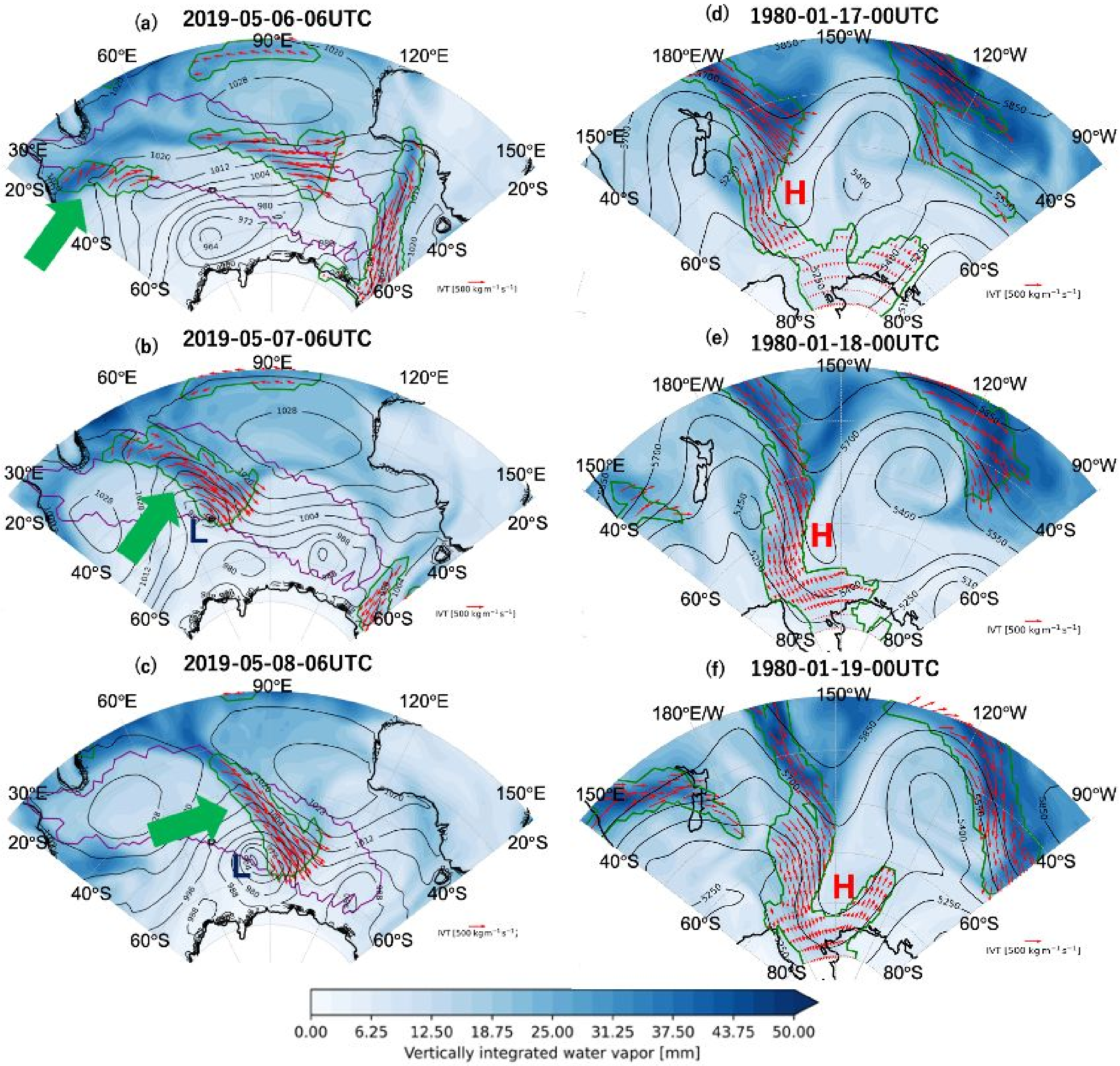

Fig. 2 Example of ARs observed over (a-c) May 6th-8th, 2019 and (d-f) January 17th-19th, 1980. Green contours denote the detected AR area, while black contours show surface pressure for (a-c) and geopotential height at 500 hPa for (d-f). Blue shading shows vertically integrated water vapor (blue shade; unit: mm) while red arrows represent vertically integrated water vapor flux (red arrows; unit: $\mathrm{kg\,m^{-1}s^{-1}}$) (the vectors are drawn within the AR region only). For (a-c), purple contour represents an outline of the footprint of the AR around at 30°E and 20°S at 06 UTC on May 6th, 2019 (denoted by green arrow) (purple contours are identical for three panels).

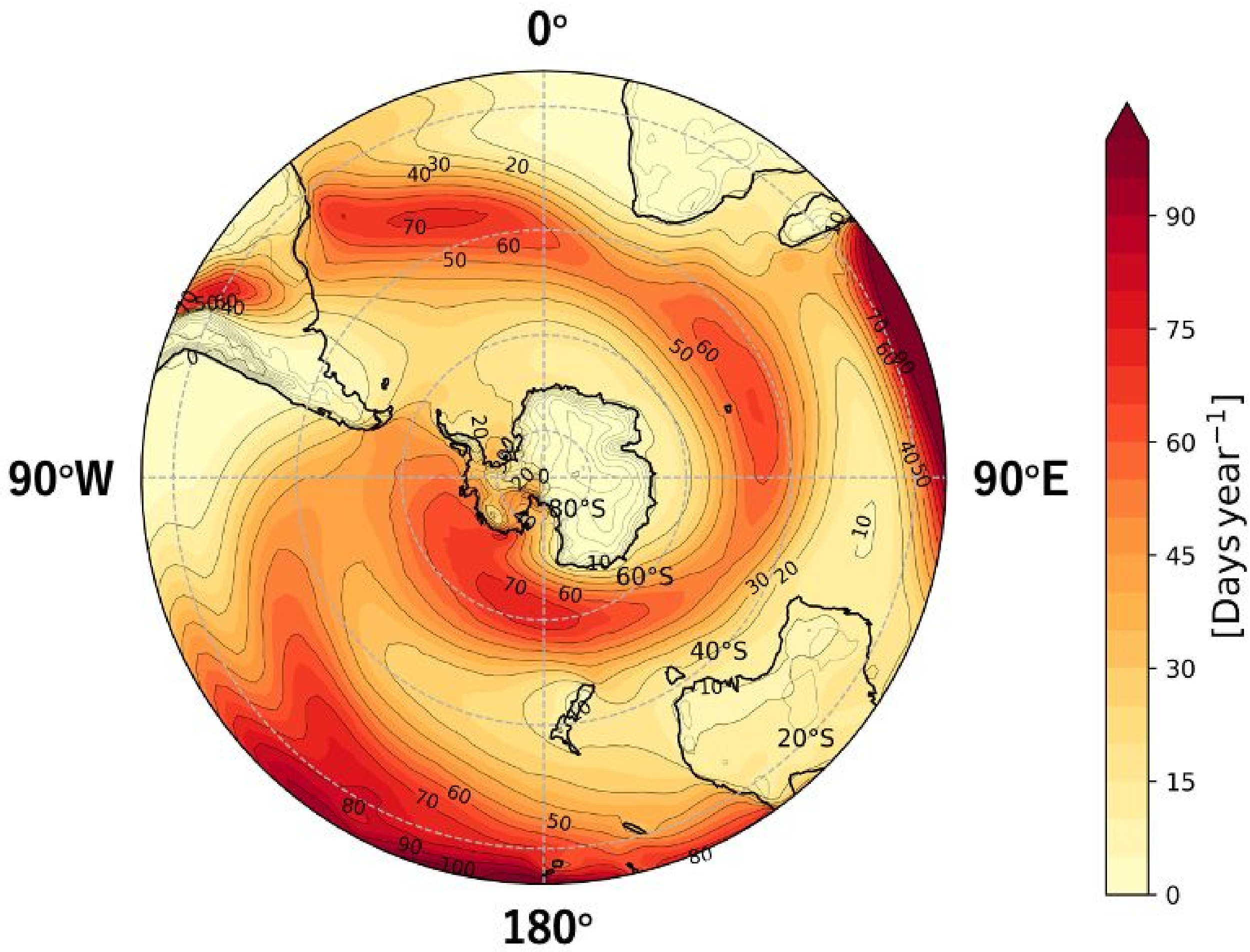

Fig. 3 The annual-mean AR frequency of AR detection (color and black contours; unit: days year^{-1}). Thin black curves over the continent indicate the topography with the contour interval of 500 m.

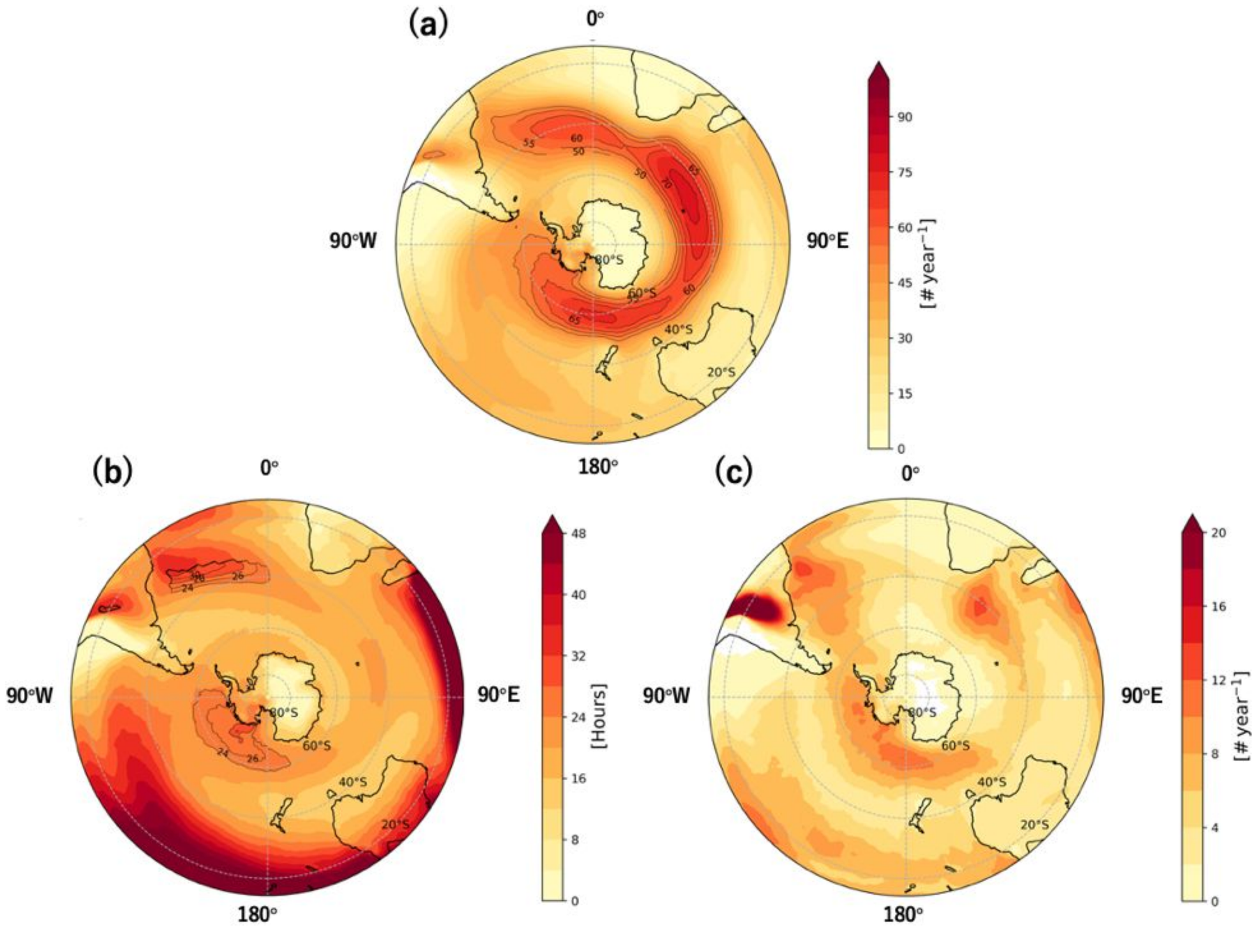

Fig. 4 (a) As is Fig. 2, but for the number of AR occurrences (color and black contour; unit: year^{-1}) which is derived by the AR tracking. (b) The persistence of the ARs (unit: Hours) which is calculated as the AR frequency divided by the AR occurrence. Contours are shown only for the region where ARs occurrence frequency is more than 50 year^{-1} and persisted for more than a day. (c) As in Fig. 3a, but for the result with only AR objects at the first time step of tracking being considered (unit: year^{-1}), indicating the source region of the AR.

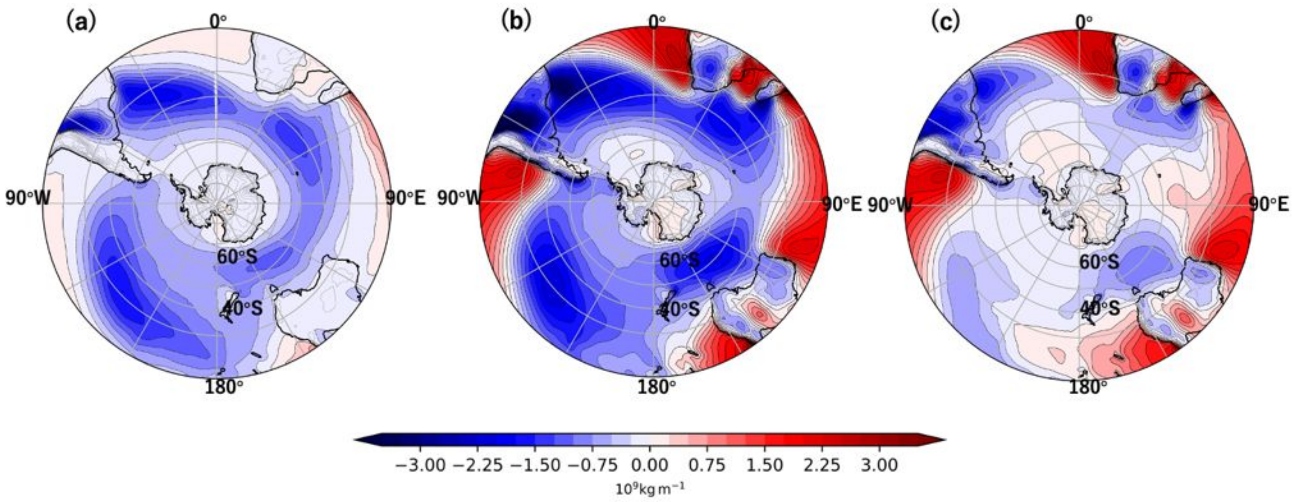

Fig. 5 (a) Meridional moisture transport related to AR, i.e. the meridional moisture transport occurring within ARs, (b) Total meridional moisture transport, and (c) the difference between the two (unit: $\mathrm{kg\,m^{-1}}$). Negative values (blue color) indicate that the direction is southward.

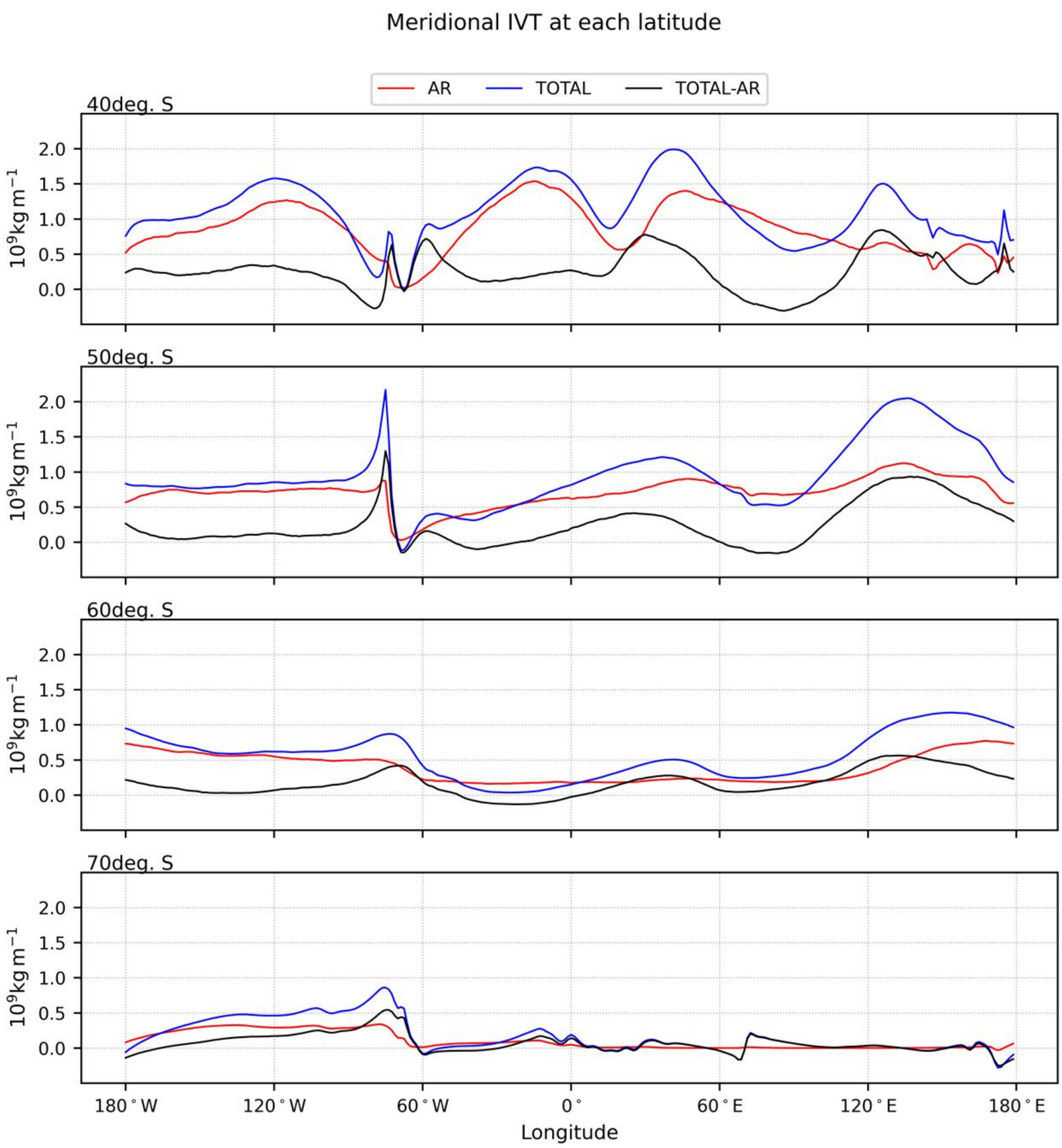

Fig. 6 The longitudinal distribution of meridional moisture transport related to AR (red line), Total (blue line), and the difference between the two(black line) at 40°, 50°, 60°, and 70°S, respectively (unit: $\mathrm{kg\,m^{-1}}$).

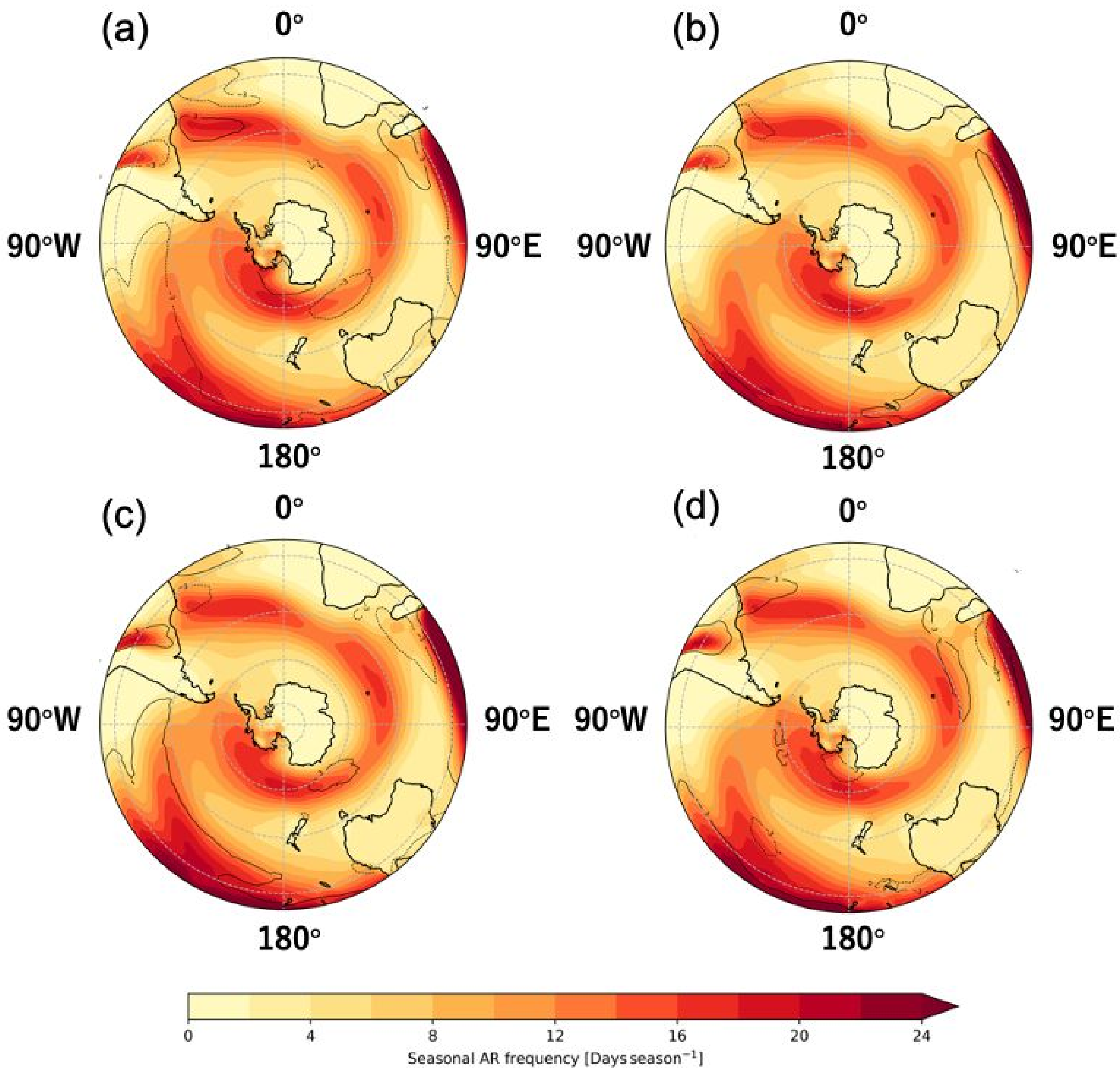

Fig. 7 As is Fig. 2, but for the seasonal-mean for (a) DJF (from December to February), (b) MAM (from March to May, (c) JJA (from June to August), and (d) SON (from September to November) (unit: $\mathrm{days\ season^{-1}}$). Contours indicate the anomaly the annual-mean (%): solid and dashed ones showing the positive and negative anomaly, respectively. The contour interval is 3%.

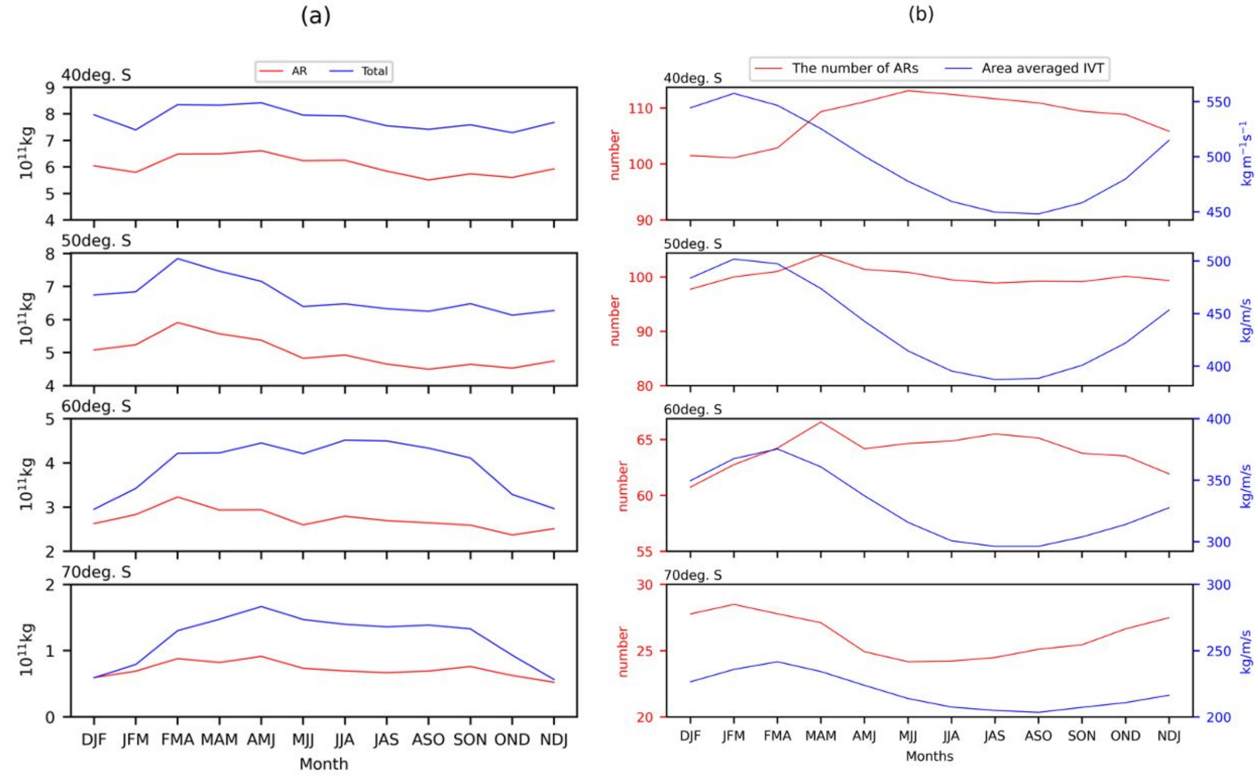

Fig. 8 (a) Seasonal variability of 3-month mean southward moisture transport by AR (red line) and that of total moisture transport (blue line) at four different latitudes (unit: kg). (b) As is panel a, but for the number of ARs (red line; unit: $3\mathrm{months}^{-1}$) and the ARs' area-averaged IVT (blue line; unit: $\mathrm{kg\,m^{-1}s^{-1}}$) the ARs reaching the latitude are considered for the analysis.

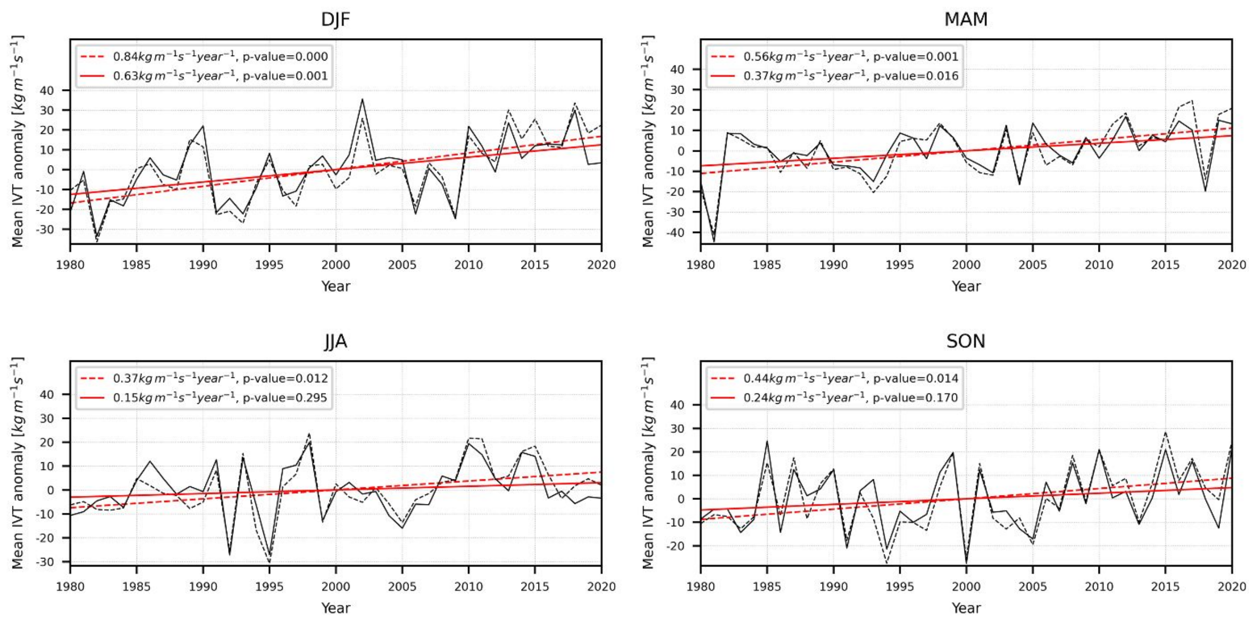

Fig. 9 Seasonal mean IVT anomaly of ARs (unit: $\mathrm{kg\,m^{-1}s^{-1}}$) across 60°S between 1980 and 2020 (black line) and its linear trend (red line) in DJF, MAM, JJA, and SON. The *p*-values are shown in the upper-left of each panel. The solid lines show the results from

JRA55, and the dashed lines show the results from ERA5.

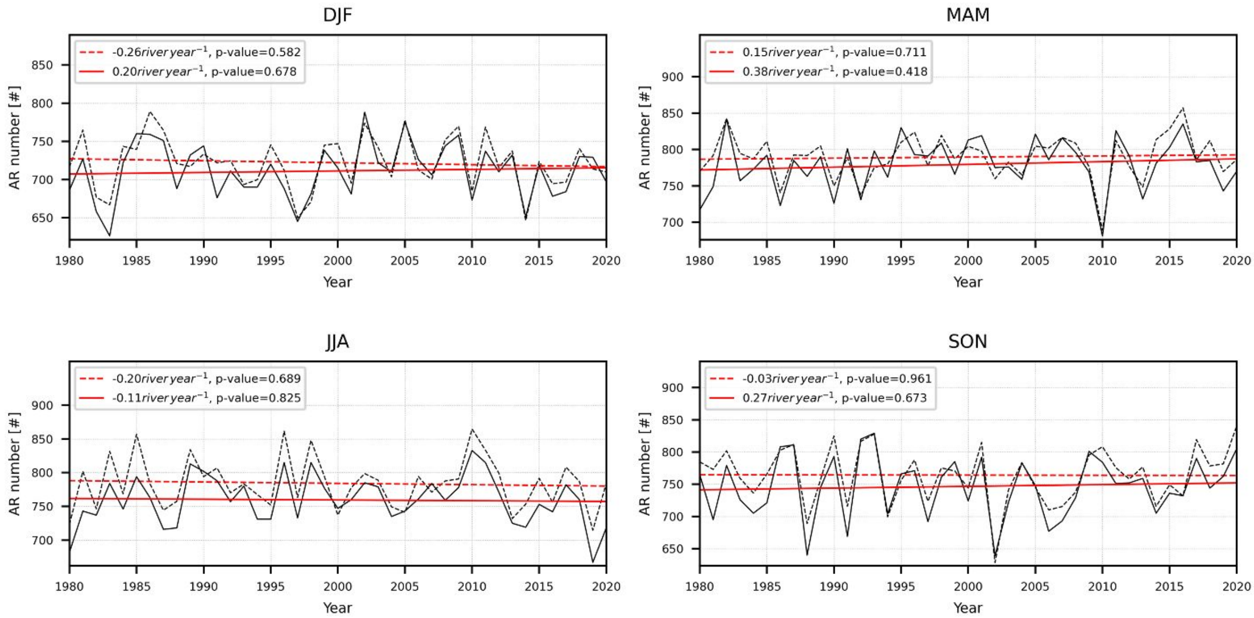

Fig. 10 As is Fig. 9, but for the number of ARs detection at 60°S.

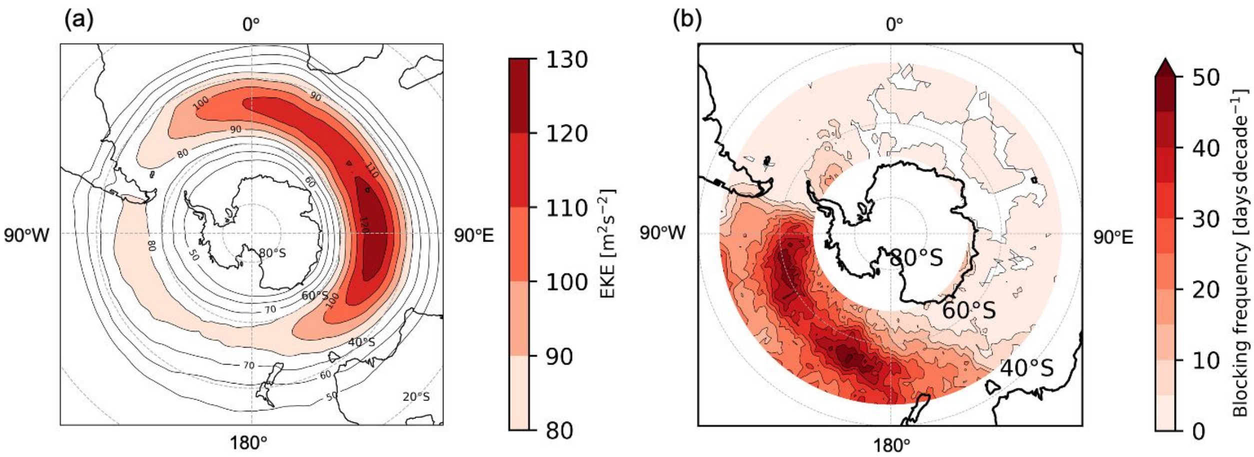

Fig. 11 (a) Annual mean 300-hPa synoptic-scale EKE (unit: unit: m^2s^{-2}). Contour interval is 10 m^2s^{-2}. (b) Number of blocking high occurrence (unit: days decade^{-1}). Contour interval is 5 days decade^{-1}.

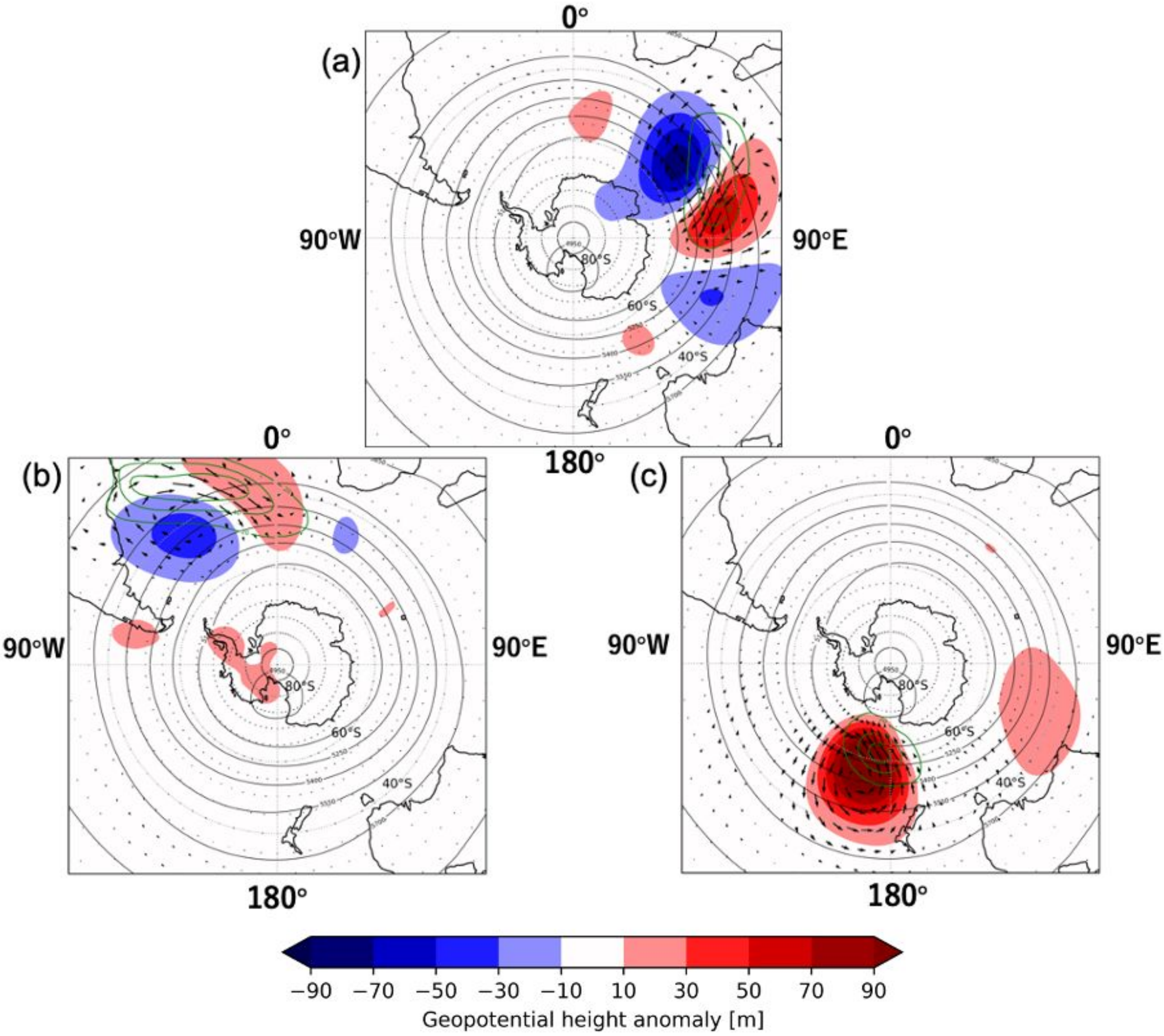

Fig. 12 Composite-mean 500hPa geopotential height anomalies (color shades; unit: m) from the climatology for 41 years (black contours; unit: m) when ARs are detected in the region where the detection frequency is maximum (green contours; unit: $days\ year^{-1}$) in (a) the Indian, (b) Atlantic, and (c) Pacific Oceans. Vectors indicate the IVT anomaly from its climatology for 41 years (unit:$kg\ m^{-1}s^{-1}$). The color interval is 20 m, and contour interval is 150 m.

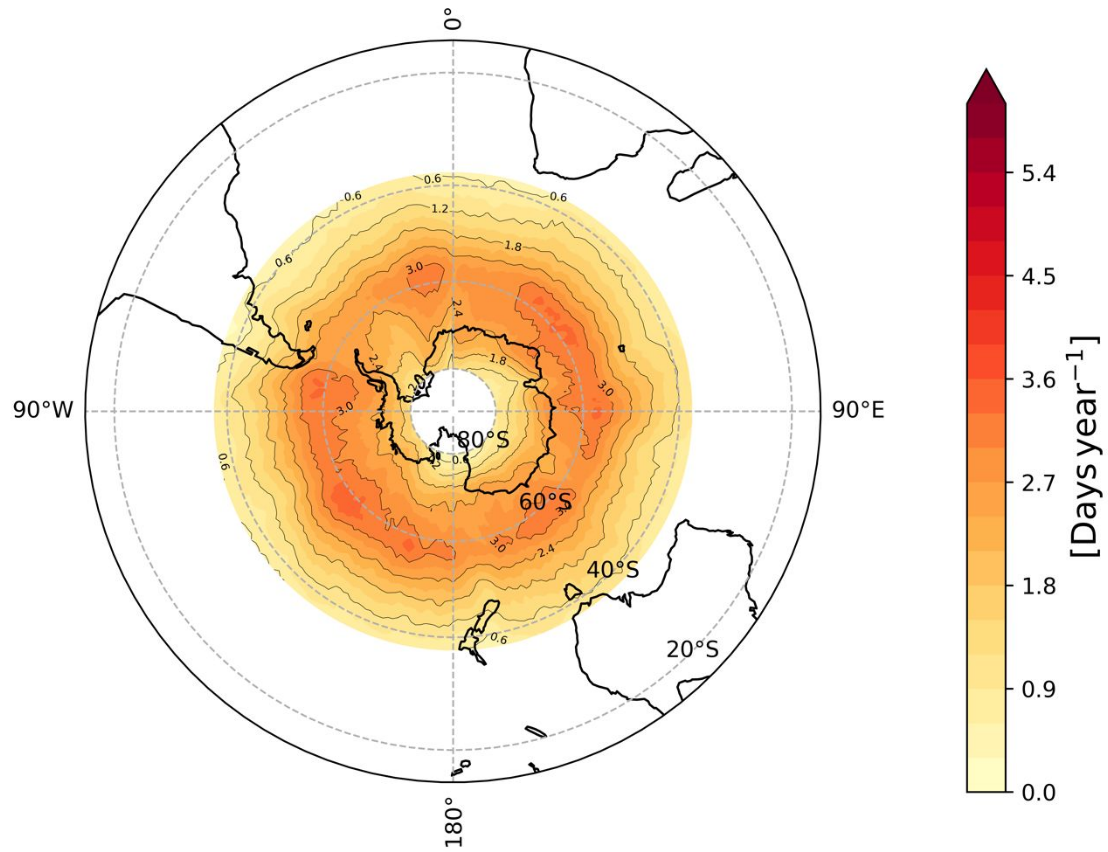

Fig. A1 The annual mean AR frequency (color and black contours; unit: $\mathrm{days\ year^{-1}}$) based on the AR detection algorithm used by Wille et al. (2021).

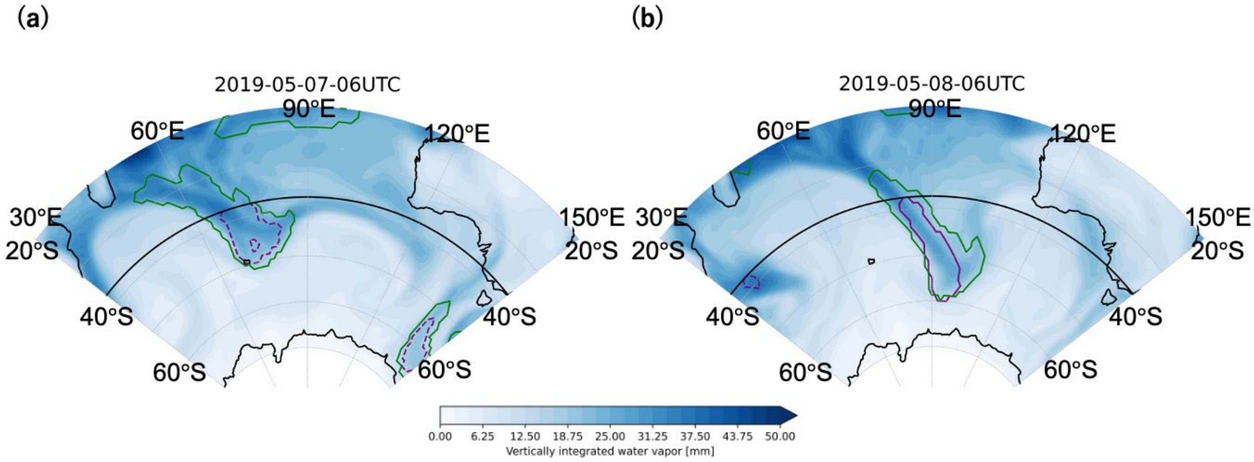

Fig. A2 The ARs detected by the present algorithm (green contour), and those detected by Wille et al. (2021) (purple solid contours), and AR-candidate before applying geometric requirement in the algorithm used by Wille et al. (2021) (green dashed contour). Blue shade indicates the vertically integrated water vapor (mm). The thick black line indicates the boundary at 37.5°S of the domain where the AR detection algorithm used by Wille et al., 2021 performs.

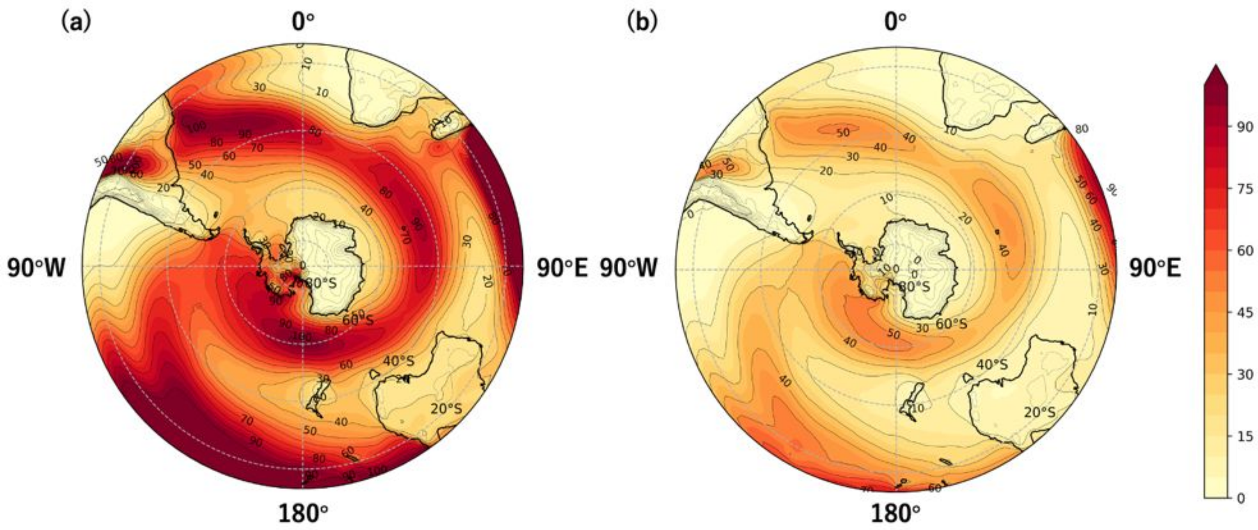

Fig. B1 The AR detection frequency based on the algorithm, which is same as that used in this study, but for the different thresholds of (a) 20% and (b) 30% of the maximum zonal anomaly of IVT at each latitude.

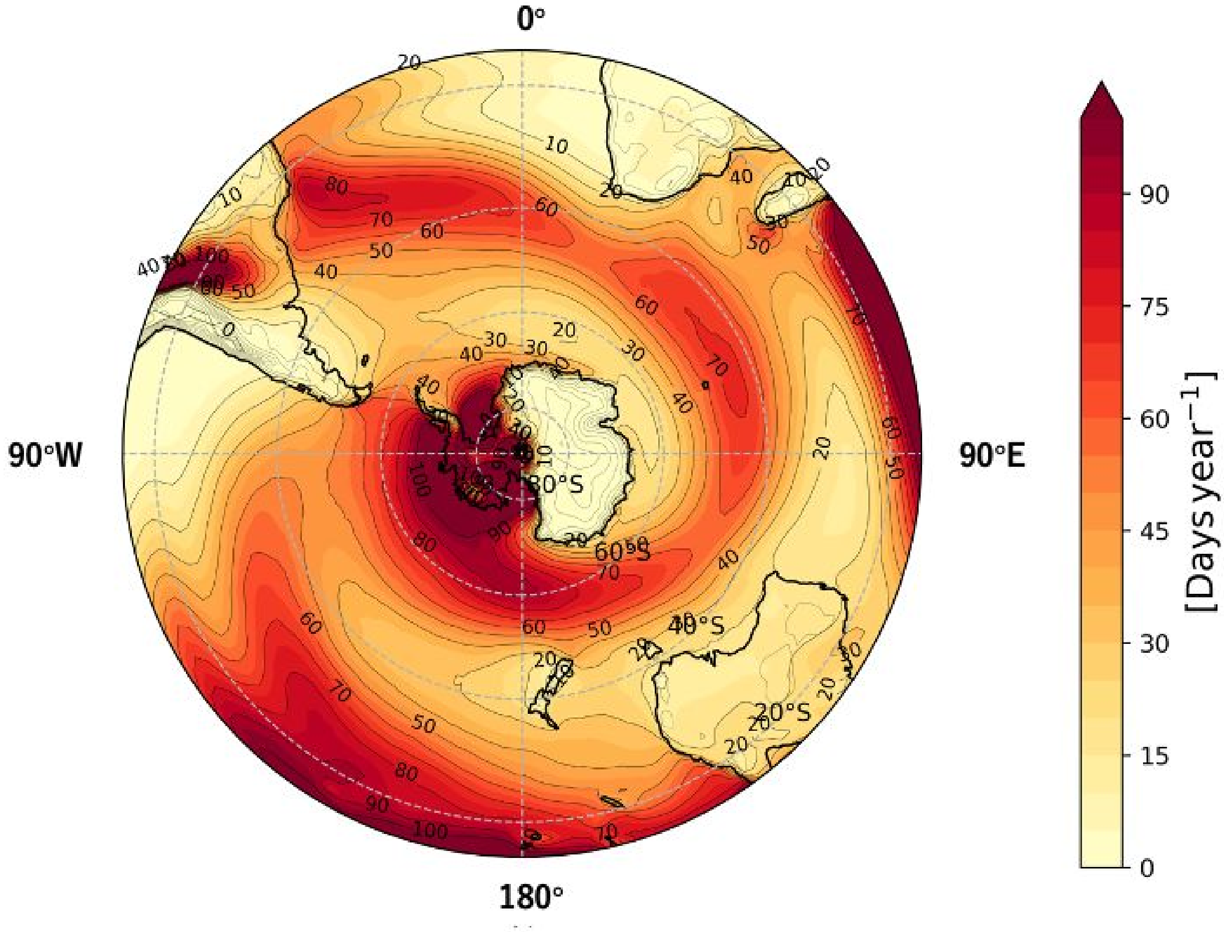

Fig. B2 AR detection frequency without applying geometric requirements in the AR detection algorithm used in the present study (color and black contours; unit: $\mathrm{days\ year^{-1}}$).